Possible Néel orderings of the Kagomé antiferromagnet

A. B. Harris

Department of Physics, University of Pennsylvania, Philadelphia, Pennsylvania 19104

C. Kallin* and A. J. Berlinsky*

Department of Physics, University of British Columbia, Vancouver, British Columbia, Canada V6T 2A6

(Received 19 August 1991)

Possible Néel orderings of antiferromagnetically coupled spins on a kagomé lattice are studied using linear-spin-wave theory and high-temperature expansions. Spin-wave analysis, applied to $q=0$ (three spins per magnetic unit cell) and to $\sqrt{3} \times \sqrt{3}$ (nine spins per cell) Néel orderings yield identical excitation spectra with twofold-degenerate linear modes and a dispersionless zero-energy mode. This dispersionless mode is equivalent to an excitation localized to an arbitrary hexagon of nearest-neighbor spins. Second- (J_2) and third- (J_3) neighbor interactions are shown to stabilize the $q=0$ state for $J_2 > J_3$ and the $\sqrt{3} \times \sqrt{3}$ state for $J_2 < J_3$. A high-temperature expansion of the spin-spin susceptibility $\chi_{\alpha\beta}(q)$ is performed to order $1/T^8$, for n-component, classical spins with nearest-neighbor interactions only. To order $1/T^7$ the largest eigenvalue of the susceptibility matrix is found to be independent of wave vector with an eigenvector that corresponds to the dispersionless mode of the ordered phase. This degeneracy is removed at order $1/T^8$. For $n=0$, the $q=0$ mode is favored; for $n=1$, the band is flat; and for $n > 1$, the maximum susceptibility is found for a $\sqrt{3} \times \sqrt{3}$ excitation. Similar results are found for the three-dimensional pyrochlore lattice. The high-temperature expansion is used to interpret experimental data for the uniform susceptibility and powder-neutron-diffraction spectrum for the kagomé-lattice system $SrCr_{8-x}Ga_{4+x}O_{19}$.

I. INTRODUCTION

The ordering of antiferromagnetically coupled Heisenberg spins in solids is usually some kind of Néel ordering in which the average sublattice magnetization per site is nonzero at low temperatures in three dimensions[1] and at $T=0$ in two dimensions.[2] In one dimension, by contrast, the average sublattice magnetization is zero even at $T=0$ although short-range antiferromagnetic correlations can be quite large.[3] The ground state of quantum Heisenberg antiferromagnets with nearest-neighbor exchange in one dimension is a kind of "spin liquid" which is incompressible (i.e., which exhibits a gap in the excitation spectrum) for integer spin[4] and compressible (gapless) for half-integer spin.[5] Quite generally in any dimension, one expects the quantum antiferromagnet (QAFM) to have either a unique ground state or a finite number of equivalent ground states, that is, that the entropy per site at $T=0$ will be zero.

Possible orderings in the ground state of a QAFM include Néel, helical,[6,7] spin liquid,[4,5,7,8] spin nematic,[9] dimer,[7,10,11] or chiral liquid.[12,13] The triangular QAFM is thought to exhibit long-range Néel order at $T=0$ (Ref. 14) of the type shown in Fig. 1(a) for large spin S and possibly even for $S=\frac{1}{2}$, although this last statement is by no means proven.[13] Dimer ordering is found for various SU(n) models for large n and may survive in the limit $n \to 2$, i.e., for $S=\frac{1}{2}$, for models with competing further-neighbor interactions.[7,10] There are no proven examples of spin liquid or dimer ground states for the Heisenberg QAFM in $d > 1$, but likely candidates would appear to be highly frustrated lattices with small coordination numbers such as the kagomé [Fig. 1(a)] and pyrochlore[11] (Fig. 2) in which the classical Heisenberg AFM is highly degenerate and hence no particular Néel ordering is favored. Clearly, to determine the ground state of the QAFM on such highly frustrated lattices one will have to
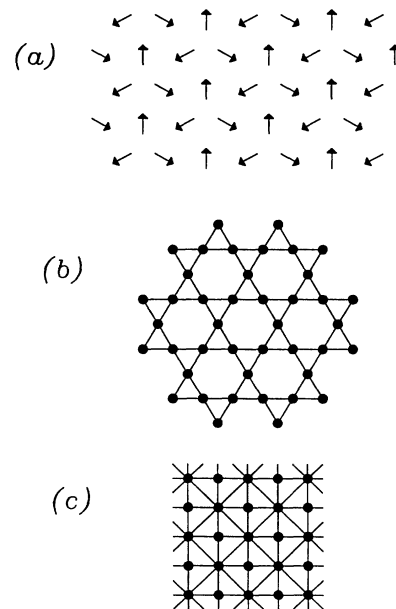

FIG. 1. Some two-dimensional lattices for which the nearest-neighbor Ising antiferromagnet exhibits finite ground-state entropy: (a) triangular, (b) kagomé, and (c) Union Jack. The vector spins in (a) correspond to one of the ground states of the XY or Heisenberg models on this lattice.

estimate the energy of the Néel ordered state on these structures to be in a position to compare it to the energy of any of the special quantum ground states mentioned above.

Even determining the Néel ground state for an AFM on such highly frustrated lattices is nontrivial. In fact, for classical Hamiltonians, such as the Ising and the classical XY and Heisenberg antiferromagnets the ground-state manifolds may have a nonzero entropy per site. This is the case, for instance, for the Ising antiferromagnet (AFM) on a number of two-dimensional lattices (e.g., triangular, kagomé, Union Jack, etc., see Fig. 1). These systems are disordered at $T=0$ and have finite ground-state entropy.[15] The frustration which disorders the triangular Ising AFM is somewhat relieved for the classical XY and Heisenberg AFM's which order in the Néel state shown in Fig. 1(a).[16] However, for other lattices, such as the kagomé in 2D and the pyrochlore (Fig. 2) in 3D, the classical Heisenberg AFM is probably disordered at $T=0$, as is suggested by mean-field[17] and Monte Carlo calculations.[18] However, the situation is not entirely clear, because even for classical systems, one can expect removal of degeneracy when fluctuations beyond mean-field theory are taken into account.

In principle, after the ground-state manifold is determined, one can then study how fluctuations resolve the degeneracy within this manifold.[19] There have been a number of studies which show how quantum[20,21] or thermal[22] fluctuations can remove classical or mean-field degeneracies between inequivalent structures. In such cases one is usually faced with considering the competition between different structures in a relatively restricted manifold. In the early calculation of Shender,[20] the degeneracy was with respect to a single angle between two sublattices which were uncoupled in a mean-field sense. In that case one has a degeneracy at one point in the Brillouin zone where a mean-field treatment predicts no gap in the excitation spectrum, but where quantum fluctuations lead to a nonzero gap. More recently, removal of degeneracy of soft lines (i.e., an excitation spectrum with no gap along a particular direction in the Brillouin zone) has been studied in the context of a model with competing interactions between nearest and further neighbors.[6,23] In the present case, the physics may be similar, but here our spin-wave calculations indicate a much more pathological scenario involving the existence of a soft zone. Such a result was previously obtained for the sus-
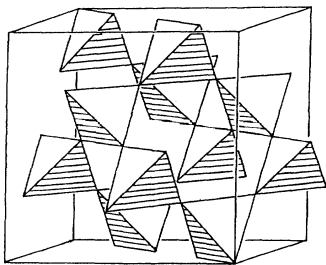
ceptibilities of both the kagomé and pyrochlore lattices[17] and is implicit in the results of the spin-wave calculations of Zeng and Elser.[24] Here we analyze two candidate structures for the kagomé lattice. We find that in both structures the noninteracting spin-wave spectrum is gapless throughout the Brillouin zone. This degeneracy can be trivially removed by considering further-than-nearest-neighbor interactions. It can also be removed by considering quantum fluctuations, and we are currently carrying out such calculations. Here however, we present a simple calculation which shows how thermal fluctuations remove the degeneracy over the entire zone. This calculation consists of a high-temperature expansion to incorporate in a controlled way the effect of thermal fluctuations. Indeed we find that in general there is a removal of degeneracy, but it only occurs at rather high order in the expansion. Thus the quantitative effect of this removal of degeneracy is not so easy to analyze.

Physical examples of the kagomé structure include second layer ^{3}He on graphite[25,26] and the stacked kagomé system, $SrCr_{8-x}Ga_{4+x}O_{19}$.[27,28] These latter compounds exhibit diffuse neutron scattering over a broad temperature regime. Obradors[27] has emphasized the very large values of the ratio, f, of the Curie temperature to the ordering temperature in this material. Another family of stacked kagomé layers were the jarosites,[29] $MFe_3(OH)_6(SO_4)_2$, where M can be H_3O, Na, K, Rb, Ag, NH_4, Tl, Pb, or Hg.

Experimental realizations of the pyrochlore structure include $CsMFeF_6$, $M=Mn$ or Ni,[30] and the class of compounds, $R_2M_2O_7$, where R is a rare-earth atom and M is Mn or Mo.[31] These compounds are described as exhibiting "spin-glass-like" behavior, including large entropy removal at low temperature with no associated sharp phase transition, irreversibilities in dc magnetization, frequency dependence in the ac susceptibility, and diffuse neutron scattering over a wide temperature range in the absence of any magnetic Bragg peaks.[18,30,31]

The studies described in this paper are intended to give some insight into the possible orderings of the Heisenberg AFM on a kagomé lattice. The results are derived from two kinds of calculations. The first, described in Sec. II is a linear-spin-wave analysis of two possible Néel states of the spin-S Heisenberg QAFM. (See Fig. 3.) One of these is a $q=0$ state in which the three sublattices of the kagomé contain spins oriented 120° apart. The other is a $\sqrt{3}\times\sqrt{3}$ structure, considered by earlier authors,[24] containing nine sublattices, which is obtained from the ordering triangular structure by deleting one-quarter of the spins, corresponding to the hexagon centers of the kagomé. For nearest-neighbor interactions only, the linear spin-wave spectra for these two ordered states are identical, and each exhibits a zero-energy dispersionless mode, which we identify as a zero-energy local excitation of the spins, with alternating sign, around any hexagon. Inclusion of second- and third-neighbor interactions (J_2 and J_3) stabilizes the excitation spectrum of the $q=0$ state for $J_2-J_3>0$ and that of the $\sqrt{3}\times\sqrt{3}$ state for $J_2-J_3<0$.

The second calculation presented in Sec. III is a high-temperature expansion of the wave-vector-dependent susceptibility $\chi_{\alpha\beta}(\mathbf{q})$ for n-component classical vector spins,
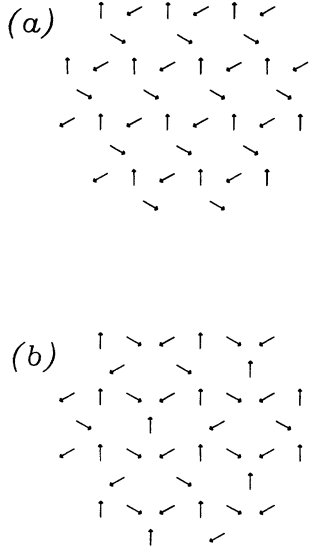

FIG. 2. The three-dimensional pyrochlore lattice of corner-sharing tetrahedra.

FIG. 3. Two possible Néel states of the kagomé lattice: (a) a $q=0$ state in which spins on each of the sublattices are parallel to each other and make an angle of 120° with the spins on the other two sublattices and (b) a $\sqrt{3}\times\sqrt{3}$ structure which is obtained by deleting $\frac{1}{4}$ of the ordered spins of a triangular lattice to form a kagomé lattice.

to order β^8 in powers of the inverse temperature β. For the kagomé lattice, $\chi_{\alpha\beta}(\mathbf{q})$ is a 3×3 matrix for each $\mathbf{q}$. The eigenvalues of this matrix are the susceptibilities of "normal modes" of the disordered state. The remarkable result which we obtain is that the largest eigenvalue of $\chi_{\alpha\beta}(\mathbf{q})$ is independent of $\mathbf{q}$ to order β^7. The condition for the $\mathbf{q}$ independence of this mode of $\chi_{\alpha\beta}(\mathbf{q})$ is shown to be that the position-space susceptibility χ_{ij} gives zero when j is summed, with alternating sign, around any hexagon not containing site i. For $n\neq1$ this condition is first violated in eighth order in the high-temperature expansion. We find that the wave function at which the susceptibility is maximal is $q=0$ for $n=0$ (which describes self-avoiding walks[32]) and for $n>1$ is $\mathbf{q}=\mathbf{q}_{\sqrt{3}}$, the wave vector of the $\sqrt{3}\times\sqrt{3}$ structure. We find a similar result for the three-dimensional pyrochlore lattice.

In Sec. IV the calculated susceptibility is used to interpret experimental data for the uniform magnetic susceptibility and for the powder-neutron-diffraction spectrum of $SrCr_{8-x}Ga_{4+x}O_{19}$.[28] The paper concludes with a summary and discussion of the main results of the paper and of the implications of the present calculations for understanding the possible ground states of the quantum cases, $S=\frac{1}{2},1$, etc.

II. LINEAR-SPIN-WAVE THEORY

The Hamiltonian, including further neighbor interactions, has the form

$$H=\frac{1}{2}\sum_{\mathbf{R},\alpha}\sum_{\mathbf{R}',\beta}J(\mathbf{R}+\mathbf{r}_\alpha-\mathbf{R}'-\mathbf{r}_\beta)\mathbf{S}_{\mathbf{R},\alpha}\cdot\mathbf{S}_{\mathbf{R}',\beta} , \tag{2.1}$$

where $\mathbf{R}$ and $\mathbf{R}'$ are lattice vectors of the triangular lat-

tice with lattice constant $2a$ (a is the nearest-neighbor separation), and the $\mathbf{r}_\alpha$ are sublattice vectors, $\mathbf{r}_1=(a,0)$, $\mathbf{r}_2=(a/2,-\sqrt{3a/2})$, $\mathbf{r}_3=(0,0)$. Henceforth we will set $a=1$. The kagomé lattice and basis vectors are shown in Fig. 4. We consider Néel states in which neighboring spins are oriented 120° apart from some plane taken to be the x-z plane in spin space. We call the three orientations A, B, and C and write spins in the crystal frame in terms of spin components referred to these local axes (indicated by tildes) as follows:

$$\mathbf{S}_A=(\tilde{S}^x_A,\tilde{S}^y_A,\tilde{S}^z_A) ,$$

$$\mathbf{S}_B=\left[-\frac{1}{2}\tilde{S}^x_B+\frac{\sqrt{3}}{2}\tilde{S}^z_B, \tilde{S}^y_B, -\frac{\sqrt{3}}{2}\tilde{S}^x_B-\frac{1}{2}\tilde{S}^z_B\right] ,$$
$$\tag{2.2}$$

$$\mathbf{S}_C=\left[-\frac{1}{2}\tilde{S}^x_C-\frac{\sqrt{3}}{2}\tilde{S}^z_C, \tilde{S}^y_C, \frac{\sqrt{3}}{2}\tilde{S}^x_C-\frac{1}{2}\tilde{S}^z_C\right] .$$

The simplest case to consider is the $\mathbf{q}=0$ Néel state in which spins on sublattices 1, 2, and 3 are of type A, B, and C, respectively. Writing

$$H=H_1+H_2+H_3 , \tag{2.3}$$

where H_n involves only nth-neighbor interactions, then for $n=1$ and 2:

$$H_n=\frac{1}{2}J_n\sum_{\mathbf{R},\alpha}\sum_{\mathbf{R}',\beta}{}^{(n)}\left[-\frac{1}{2}\tilde{S}^x_{\mathbf{R},\alpha}\tilde{S}^x_{\mathbf{R}',\beta}+\tilde{S}^y_{\mathbf{R},\alpha}\tilde{S}^y_{\mathbf{R}',\alpha}\right.$$
$$-\frac{1}{2}\tilde{S}^z_{\mathbf{R},\alpha}\tilde{S}^z_{\mathbf{R}',\beta}$$
$$+\sin\frac{2\pi}{3}(\alpha-\beta)(\tilde{S}^x_{\mathbf{R},\alpha}\tilde{S}^z_{\mathbf{R}',\alpha}$$
$$\left.-\tilde{S}^z_{\mathbf{R},\alpha}\tilde{S}^x_{\mathbf{R}',\beta})\right] ,$$
$$\tag{2.4}$$

where the (n) over the second sum restricts $\mathbf{R}+\mathbf{r}_\beta$ to be an nth neighbor of $\mathbf{R}+\mathbf{r}_\alpha$. For third neighbors ($n=3$),

$$H_3=\frac{1}{2}J_3\sum_{\mathbf{R},\alpha}\sum_{\mathbf{R}'}{}^{(3)}\tilde{S}_{\mathbf{R},\alpha}\cdot\tilde{S}_{\mathbf{R},\alpha} , \tag{2.5}$$
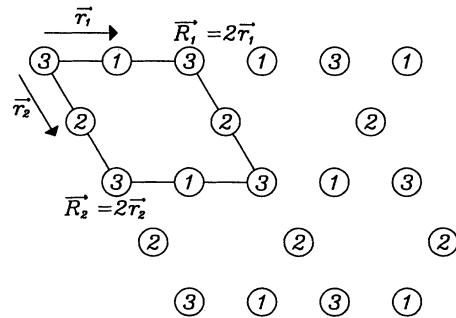

FIG. 4. Kagomé lattice with sublattices labeled to correspond to the $q=0$ structure. The basis vectors for the $q=0$ structure are $\mathbf{r}_1$, $\mathbf{r}_2$, and $\mathbf{r}_3=0$. The Bravais lattice vectors are $\mathbf{R}_1=2\mathbf{r}_1$ and $\mathbf{R}_2=2\mathbf{r}_2$.

since third neighbors lie on the same sublattice for this choice of Néel state. Note that there are two inequivalent sets of third neighbors in the kagomé lattice, one reached by two nearest-neighbor steps and the other (on opposite sides of a hexagon) by three. Here J_3 refers to coupling of the first type, and the latter coupling is ignored.

The linearized Holstein-Primakoff transformation to boson spin-wave operators is

$$\tilde{S}^x_{R,\alpha} = \sqrt{S/2}[c^\dagger_\alpha(R) + c_\alpha(R)] \ ,$$

$$\tilde{S}^y_{R,\alpha} = i\sqrt{S/2}[c^\dagger_\alpha(R) - c_\alpha(R)] \ , \qquad (2.6)$$

$$\tilde{S}^z_{R,\alpha} = S - c^\dagger_\alpha(R)c_\alpha(R) \ .$$

The Néel state energy per spin for this case is

$$E_0/(3N) = -(J_1 + J_2 - 2J_3)S^2 \ , \qquad (2.7)$$

where N is the number of unit cells, and the harmonic spin-wave Hamiltonian is

$$H^{(2)} = \frac{1}{4}S \sum_{k,\alpha,\beta} \{\gamma^{(1)}_{\alpha\beta}(k)c^\dagger_\alpha(k)c_\beta(k) + \gamma^{(2)}_{\alpha\beta}(k)$$

$$\times [c^\dagger_\alpha(k)c^\dagger_\beta(-k) + c_\alpha(-k)c_\beta(k)]\} \ , \qquad (2.8)$$

where the $c^\dagger_\alpha(k)$ are defined by

$$c^\dagger_\alpha(R) = \frac{1}{\sqrt{N}} \sum_k c^\dagger_\alpha(k)e^{-ik\cdot(R+r_\alpha)} \ , \qquad (2.9)$$

and

$$\gamma^{(1)}_{\alpha\alpha}(k) = 8(J_1 + J_2) - 16J_3\left[1 - \frac{1}{2}\sum_{\beta\neq\alpha}\cos 2k\cdot(r_\beta - r_\alpha)\right] \ ,$$

$$\gamma^{(2)}_{\alpha\alpha}(k) = 0 \ ,$$

$$\gamma^{(1)}_{\alpha\beta}(k) = 2J_1\cos k\cdot(r_\beta - r_\alpha) + 2J_2\cos k\cdot(r_\alpha + r_\beta - 2r_\gamma) \ ,$$

$$\gamma^{(2)}_{\alpha\beta}(k) = -\frac{3}{2}\gamma^{(1)}_{\alpha\beta}(k) \ , \qquad (2.10)$$

where the subscripts α, β, and γ must all be different.

It is instructive to consider the nearest-neighbor case $J_2 = J_3 = 0$ and $J_1 = J$. Then

$$H^{(2)} = \frac{1}{4}JS \sum_{k,\alpha,\beta} \{(8\delta_{\alpha\beta} + 2\Lambda_{\alpha\beta})c^\dagger_\alpha(k)c_\beta(k) - 3\Lambda_{\alpha\beta}$$

$$\times [c^\dagger_\alpha(k)c^\dagger_\beta(-k) + c_\alpha(k)c_\beta(-k)]\} \ , \qquad (2.11)$$

where

$$\Lambda = \begin{vmatrix} 0 & \cos(q_1 - q_2) & \cos q_1 \\ \cos(q_1 - q_2) & 0 & \cos q_2 \\ \cos q_1 & \cos q_2 & 0 \end{vmatrix} \ , \qquad (2.12)$$

and $q_1 = k_x$, $q_2 = (k_x - \sqrt{3}k_y)/2$. The matrix Λ has eigenvalues

$$\lambda_1 = -1 \ , \qquad (2.13)$$

$$\lambda_{2,3} = \frac{1}{2}\{1 \pm \sqrt{4[\cos^2 q_1 + \cos^2 q_2 + \cos^2(q_1 - q_2)] - 3}\} \ .$$

For eigenvalue λ the unnormalized eigenvector is

$$v(\lambda) = \begin{vmatrix} \cos q_1\cos q_2 + \lambda\cos(q_1 - q_2) \\ \lambda^2 - \cos^2 q_1 \\ \cos q_1\cos(q_1 - q_2) + \lambda\cos q_2 \end{vmatrix} \ . \qquad (2.14a)$$

For the special case $\lambda = -1$, a more convenient form of the unnormalized eigenvector is

$$v_1 = \begin{vmatrix} \sin q_2 \\ -\sin q_1 \\ \sin(q_1 - q_2) \end{vmatrix} \ . \qquad (2.14b)$$

We define the unitary transformation

$$S_{\mu\alpha}(k) = v_{\mu\alpha}/|v_\mu| \ , \qquad (2.15)$$

where $v_{\mu\alpha}$ is the α component of the eigenvector associated with λ_μ, and the operators

$$d^\dagger_\mu(k) = \sum_\alpha S_{\mu\alpha}(k)c^\dagger_\alpha(k) \ . \qquad (2.16)$$

Then $H^{(2)}$ of Eq. (2.11) becomes

$$H^{(2)} = \frac{1}{4}JS \sum_{k,\mu} \{[8 + 2\lambda_\mu(k)]d^\dagger_\mu(k)d_\mu(k) - 3\lambda_\mu(k)$$

$$\times [d^\dagger_\mu(k)d^\dagger_\mu(-k) + d_\mu(k)d_\mu(-k)]\} \ , \qquad (2.17)$$

which can be diagonalized as follows. First define momentum and coordinate operators such that $[P_\mu(k), Q_\nu(q)]_- = -i\delta_{k+q,0}\delta_{\mu,\nu}$, where δ here is the Kronecker delta:

$$Q_\mu(k) = \frac{i}{\sqrt{2}}[d_\mu(-k) - d^\dagger_\mu(k)] \ , \qquad (2.18a)$$

$$P_\mu(k) = \frac{1}{\sqrt{2}}[d^\dagger_\mu(k) + d_\mu(-k)] \ . \qquad (2.18b)$$

Then

$$H^{(2)} = \frac{1}{4}JS \sum_{k,\mu}[-(4 + \lambda_\mu) + (4 - 2\lambda_\mu)P_\mu(k)P_\mu(-k)$$

$$+ (4 + 4\lambda_\mu)Q_\mu(k)Q_\mu(-k)] \qquad (2.19a)$$

$$\equiv E_1 + \sum_\mu H^{(2)}_\mu \ , \qquad (2.19b)$$

where $E_1 = -3NJS[\sum_\mu\lambda_\mu = 0$ by Eq. (2.13)] and

$$H^{(2)}_\mu = \frac{1}{4}JS \sum_k [(4 - 2\lambda_\mu)P_\mu(k)P_\mu(-k)$$

$$+ (4 + 4\lambda_\mu)Q_\mu(k)Q_\mu(-k)] \ . \qquad (2.20)$$

Consider first the $\mu = 1$ term ($\lambda_1 = -1$),

$$H^{(2)}_1 = \frac{3}{2}JS \sum_k P_1(k)P_1(-k) \ . \qquad (2.21)$$

This Hamiltonian describes a mode with no restoring force, i.e., a zero-frequency mode for all k. We will discuss this mode in detail below, but first we consider the

Hamiltonian for modes $\mu=2,3$. Since it involves harmonic oscillators, it may be written in terms of normal mode operators which satisfy $[a_\mu(\mathbf{k}),a_\nu^\dagger(\mathbf{q})]_-=\delta_{\mathbf{k},\mathbf{q}}\delta_{\mu,\nu}$:

$$H_\mu^{(2)}=\sum_\mathbf{k}\varepsilon_\mu(\mathbf{k})[a_\mu^\dagger(\mathbf{k})a_\mu(\mathbf{k})+\tfrac{1}{2}] \qquad (2.22)$$

for $\mu=2,3$, where

$$\begin{aligned}\varepsilon_\mu(\mathbf{k})&=JS\sqrt{2[1+\lambda_\mu(\mathbf{k})][2-\lambda_\mu(\mathbf{k})]}\\&=JS\sqrt{2[\sin^2q_1+\sin^2q_2+\sin^2(q_1-q_2)]}\\&\approx JS\sqrt{3}|\mathbf{k}|, \quad |\mathbf{k}|\ll 1 \ . \qquad (2.23)\end{aligned}$$

Note that $\varepsilon_\mu(\mathbf{k})$ is the same for $\mu=2$ and 3, yielding a twofold degenerate linear mode.

Returning to the $(\mu=1)$ zero-energy mode, it is clear that such a dispersionless mode can be used to construct zero-energy local modes. Such a mode will be of the form

$$D_1^\dagger(\mathbf{R})=\frac{1}{\sqrt{N}}\sum_\mathbf{k}F(\mathbf{k})d_1^\dagger(\mathbf{k})e^{i\mathbf{k}\cdot\mathbf{R}} \ , \qquad (2.24)$$

where $F(\mathbf{k})$ is a form factor. Using Eqs. (2.9) and (2.14)–(2.16) and choosing

$$F(\mathbf{k})=2ie^{i\mathbf{k}\cdot(\mathbf{r}_1-\mathbf{r}_2)}|\mathbf{v}_1| \ , \qquad (2.25)$$

we obtain

$$\begin{aligned}D_1^\dagger=&c_3^\dagger(\mathbf{R}+\mathbf{R}_2-\mathbf{R}_1)-c_3^\dagger(\mathbf{R})+c_1^\dagger(\mathbf{R}-\mathbf{R}_1)\\&-c_1^\dagger(\mathbf{R}+\mathbf{R}_2-\mathbf{R}_1)+c_2^\dagger(\mathbf{R})-c_2^\dagger(\mathbf{R}-\mathbf{R}_1) \ . \qquad (2.26)\end{aligned}$$

The six sites associated with the operators in $D_1^\dagger(\mathbf{R})$ lie at the vertices of a hexagon centered at the point $\mathbf{R}_H=\mathbf{R}+\mathbf{r}_2-\mathbf{r}_1$ (see Fig. 5). Classically, for spins lying in the x-z plane in their Néel state, the mode $D_1^\dagger(\mathbf{R})$ corresponds to tipping spins around the hexagon alternately in and out of the plane. If the tipping angle is θ, the energy of such a mode is proportional to θ^4 with a positive coefficient. Thus in the classical case, anharmonicity apparently stabilizes the soft modes, and presumably this will also be the case for quantum spins. On the other
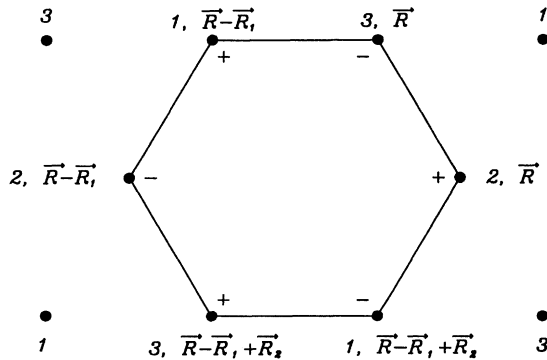

FIG. 5. The hexagon of sites involved in the right-hand side of Eq. (2.26), which describes the local zero-energy mode. The phase factors $(+)$ or $(-)$ for this mode are shown. Sites are labeled by their sublattice index, followed by the Bravais lattice vector of their unit cell.

hand, it is clear that further neighbor interactions can stabilize these modes as we shall now see.

For general J_2 and J_3, it is straightforward to show, using, for example, a generalization of the transformation (2.18), that the normal mode frequencies for the Hamiltonian of Eq. (2.8) are the positive square roots of the eigenvalues of the matrix

$$\Gamma_{\alpha\beta}=\tfrac{1}{16}S^2[(\gamma^{(1)}+2\gamma^{(2)})(\gamma^{(1)}-2\gamma^{(2)})]_{\alpha\beta} \ , \qquad (2.27)$$

where $\gamma^{(1)}$ and $\gamma^{(2)}$ are the 3×3 matrices defined in Eq. (2.10). $\Gamma_{\alpha\beta}$ can be diagonalized numerically for various values of J_2 and J_3. In addition, analytic expressions for the eigenvalues can be obtained in the long-wavelength limit. We find that for $J_2<J_3$ there are three nondegenerate linear modes with slopes (versus wave vector k) given by

$$|\varepsilon_1|/k=3S[(J_1+J_2)(J_2-J_3)]^{1/2}, \qquad (2.28a)$$

$$|\varepsilon_2|/k=S[3(J_1+J_2)(J_1+3J_2-8J_3)]^{1/2} \ , \qquad (2.28b)$$

$$|\varepsilon_3|k=S[3(J_1+J_2)(J_1-5J_3)]^{1/2} \ . \qquad (2.28c)$$

For $J_2=J_3$ the frequency of the lowest mode, ε_1, is identically zero as in the special case of $J_2=J_3=0$ considered above, and for $J_2<J_3$ this frequency is complex indicating that the $\mathbf{q}=0$ Néel state is unstable for $J_2<J_3$. In fact we shall see below that the $\sqrt{3}\times\sqrt{3}$ structure is stabilized for $J_2<J_3$. Spin-wave spectra for the case $J_2/J_1=0.05$, $J_3/J_1=0.03$ along the X and Y directions of the Brillouin zone are shown in Fig. 6.

The calculation for the $\sqrt{3}\times\sqrt{3}$ structure proceeds along the same lines as above. The energy/spin of the Néel state is

$$E_0/9N=-(J_1-2J_2+J_3)S^2 \ , \qquad (2.29)$$

where N is the number of $\sqrt{3}\times\sqrt{3}$ unit cells, each containing nine spins. Comparing to Eq. (2.7), we see that the $\sqrt{3}\times\sqrt{3}$ Néel energy is lower than that of the $\mathbf{q}=0$ state for $J_{23}<J_3$. For the linear spin-wave analysis, Eqs. (2.8) and (2.9) are unchanged except that now the sublattice indices α and β take on values 1 to 9 and the γ matrices, which become complex, must be redefined accordingly. This is easily done with the help of a diagram such as that of Fig. 7 which shows the equilibrium orientations $(A, B,$ or $C)$ and the relative positions of sublattices $1,\ldots,9$. The resulting 9×9 matrices $\gamma^{(1)}$ and $\gamma^{(2)}$ are tabulated in Appendix A. These matrices are used to construct the dynamical matrix Γ by Eq. (2.27) (which is also valid when $\gamma^{(1)}$ and $\gamma^{(2)}$ are complex Hermitian matrices), and Γ is then diagonalized numerically. The results are analogous to those of the $\mathbf{q}=0$ structure with linear modes folded back into the three times smaller Brillouin zone. However, now the slope of the two lowest "acoustic" branches is equal to $S[(J_3-J_2)(12J_1+6J_2+6J_3)]^{1/2}$, and the lowest-lying "optical" mode has a gap at zero wave vector equal to $S[(J_3-J_2)(18J_1-36J_2)]^{1/2}$. Spectra for the case $J_2/J_1=-0.05$, $J_3/J_1=-0.03$ along the X and Y directions of the Brillouin zone are shown in Fig. 8.

For the special case of nearest-neighbor interactions

only, it is shown analytically in Appendix A that the linear spin-wave spectra of the two Néel states are identical when folded into the same Brillouin zone. Hence, these two states have the same ground-state energy to order S. This energy has contributions E_1 from Eq. (2.19), zero from the ground state of $H_1^{(2)}$ in Eq. (2.21), and $\varepsilon_\mu(\mathbf{k})/2$ from the modes with $\mu=2$ or 3, so

$$\frac{E}{3N} = -JS^2 + \left[\frac{1}{2} \frac{1}{3N} \sum_\mathbf{k} \sum_{\mu=2}^3 \varepsilon_\mu(\mathbf{k}) - JS \right]$$

$$= -JS^2 - 0.4412JS \; , \qquad (2.30)$$

where $3N$ is the number of sites. For $S=\frac{1}{2}$, this energy is $-0.4706J$. Elser[26] found an upper bound of $-0.4167J$ for the ground-state energy by considering the effect of fluctuations on dimer states for $S=\frac{1}{2}$. A lower bound of $-0.5J$ follows from the solution of the three-site problem (a single plaquette) with open boundary conditions.
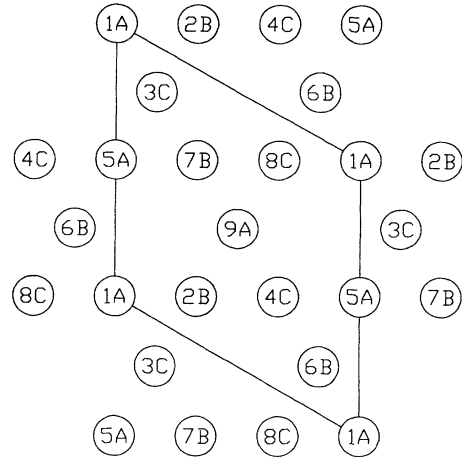

FIG. 7. Sublattice numbering $(1,2,\ldots,9)$ and spin orientations (A, B, and C) for the $\sqrt{3}\times\sqrt{3}$ Néel state. The spin orientations are those shown in the top row of spins in Fig. 3(b).
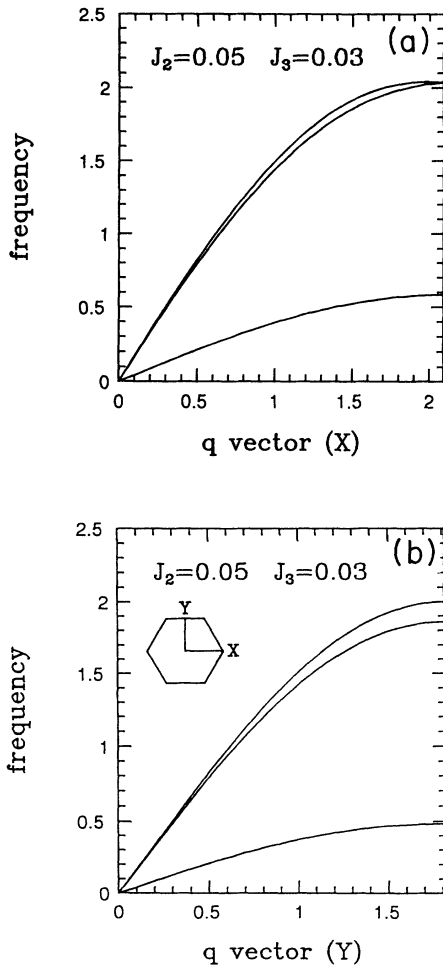

FIG. 6. Spin-wave frequencies $\varepsilon_\mu(\mathbf{q})/J_1S$ for excitations from the $\mathbf{q}=0$ state along the X and Y directions in the Brillouin zone, as indicated in the inset, for $J_1=1$, $J_2=0.05$, and $J_3=0.03$. The X point is at $(2\pi/3,0)$ and the Y point is at $(0,\pi/\sqrt{3})$. The nearest-neighbor spacing a has been set equal to 1.

FIG. 8. Spin-wave frequencies $\varepsilon_\mu(\mathbf{q})/J_1S$ for the $\sqrt{3}\times\sqrt{3}$ state along the X and Y directions in the Brillouin zone, as indicated in the inset for $J_1=1$, $J_2=-0.05$, and $J_3=-0.03$. For $\mathbf{q}$ along the Y direction, the lowest branch and the two highest branches are each twofold degenerate. The X point is at $(\pi/3,0)$ and the Y point is at $(0,2\pi\sqrt{3}/9)$. The nearest-neighbor spacing a has been set equal to 1.
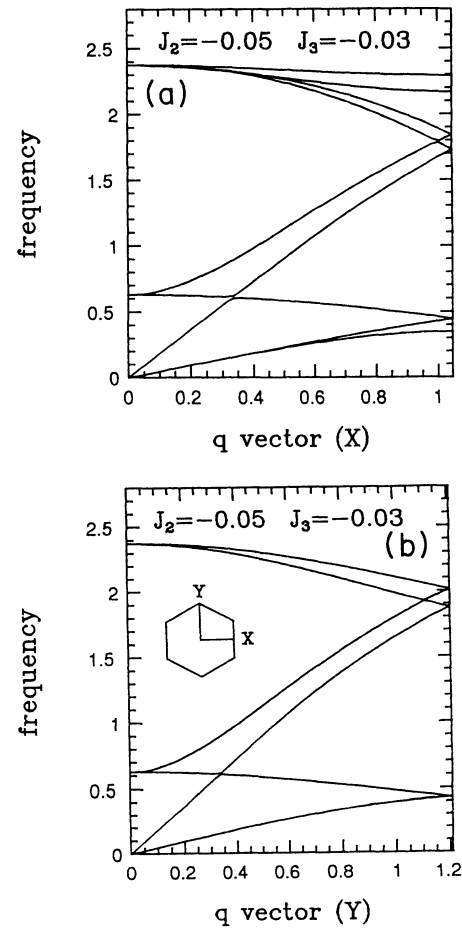
Important differences between the Néel states only arise when anharmonic effects are considered. In particular we argued above that, for classical spins the zero modes of the $q=0$ state are stabilized by fourth-order anharmonicity. On the other hand, for the $\sqrt{3}\times\sqrt{3}$ structure, cf. Fig. 7, the six spins of any hexagon involve only two of the orientations, e.g., B and C, and they are surrounded by nearest-neighbor spins of the third orientation, e.g., A. Thus, the six spins of *any* hexagon can be rotated uniformly around the third spin orientation with no cost in energy,[33] i.e., the classical restoring force for this case is zero at all orders in the rotation angle and the degenerate manifold has a finite entropy per site. We are presently studying the effects of anharmonic spin-wave interactions and quantum fluctuations on these spectra.

Our main result from this spin-wave analysis is simply that the sign of J_2-J_3 determines the relative stability of the $q=0$ and $\sqrt{3}\times\sqrt{3}$ ground states. If the mechanism for J_2 and J_3 is some kind of superexchange they could be of either sign and are likely to be very close in magnitude. Thus experimentally the condition $|J_2-J_3|/J_1\ll 1$ is quite plausible, and it is reasonable to expect that quantum effects could intervene and stabilize other kinds of ground states.

We note that Zeng and Elser[24] have performed a linear spin-wave analysis similar to ours for the $\sqrt{3}\times\sqrt{3}$ structure. Instead of including second- and third-neighbor interactions to stabilize the ground state, Zeng and Elser introduced a coupling $\tilde{J}_2$ to extra fictitious spins at the

center of each kagomé hexagon. For $\tilde{J}_2=J_1$ the problem then becomes that of the triangular antiferromagnet with nearest-neighbor couplings. For $\tilde{J}_2\to 0$, if the fictitious degrees of freedom are ignored, their numerical results tend toward our analytic results for $J_2=J_3=0$.

III. HIGH-TEMPERATURE EXPANSION OF $\chi_{\alpha\beta}(\mathbf{q})$

For nearest-neighbor couplings only, $(J_2=J_3=0)$, linear spin-wave analysis cannot distinguish between the two Néel states which were considered, except to suggest that anharmonic effects might be significant. In this section we study the susceptibility for ordering of the wave-vector-dependent magnetization, $\mathbf{S}_\alpha(\mathbf{q})$, by means of a high-temperature expansion. The virtues of this technique are (1) that it is unbiased with regard to the sublattice structure of the ordered state and (2), to whatever order it is carried, it includes all anharmonic effects.

The quantities which we need to calculate are

$$\langle \mathbf{S}_i\cdot\mathbf{S}_j\rangle_\beta=\mathrm{Tr}(\mathbf{S}_i\cdot\mathbf{S}_j e^{-\beta H})/\mathrm{Tr}\,e^{-\beta H}\ ,\tag{3.1}$$

where H is taken to include only nearest-neighbor couplings. Expanding in powers of β $(k_B=1)$ and formally dividing out the denominator gives a cumulant expansion

$$\langle \mathbf{S}_i\cdot\mathbf{S}_j\rangle_\beta=\sum_{m=0}^\infty \frac{(-\beta)^m}{m!}\langle \mathbf{S}_i\cdot\mathbf{S}_j H^m\rangle_c\ ,\tag{3.2}$$

where $\langle\ \cdots\ \rangle_c$ is a cumulant average

$$\langle ABC\cdots\rangle_c=\langle ABC\cdots\rangle_0-\sum\langle\cdots\rangle_0\langle\cdots\rangle_0$$
$$+2!\sum\langle\cdots\rangle_0\langle\cdots\rangle_0\langle\cdots\rangle_0-3!\sum\langle\cdots\rangle_0\langle\cdots\rangle_0\langle\cdots\rangle_0\langle\cdots\rangle_0+\cdots\tag{3.3}$$

and $\langle\ \cdots\ \rangle_0$ is an average (at $\beta=0$) over all orientations of the spin operators contained within the brackets. The sums, which are multiplied by $(-1)^{n-1}(n-1)!$, are over all ways that the product of the operators $\mathbf{S}_i\cdot\mathbf{S}_j$ and H can be distributed into n averages. Writing H as a sum over bonds,

$$H=J\sum_b(\mathbf{S}_{i(b)}\cdot\mathbf{S}_{j(b)})\tag{3.4}$$

and specializing to the case of classical spins so that all of the terms in H commute with each other, we obtain

$$\langle \mathbf{S}_i\cdot\mathbf{S}_j\rangle_\beta=\sum_{m=0}^\infty(-\beta J)^m\sum_{m_1,m_2,\ldots}'\frac{1}{m_1!m_2!\ldots}\langle(\mathbf{S}_i\cdot\mathbf{S}_j)(\mathbf{S}_{i(b_1)}\cdot\mathbf{S}_{j(b_1)})^{m_1}(\mathbf{S}_{i(b_2)}\cdot\mathbf{S}_{j(b_2)})^{m_2}\cdots\rangle_c\ ,\tag{3.5}$$

where the prime over the sum means that $\sum_i m_i=m$, and the product in the average is over all bonds. Because of the properties of the cumulant, only connected clusters of bonds with $m\neq 0$ will contribute to the sum in Eq. (3.5).

It is useful to represent contributions to $\langle\mathbf{S}_i\cdot\mathbf{S}_j\rangle_\beta$ diagrammatically. To each set of m_i's in Eq. (3.5) we associate a diagram, which, to avoid later confusion, we call a "simple" diagram. In a simple diagram $\mathbf{S}_i\cdot\mathbf{S}_j$ is represented by a dashed line connecting sites i and j and such a line is called an "external line." In addition, each factor of $\mathbf{S}_{i(b)}\cdot\mathbf{S}_{j(b)}$ from the Hamiltonian is represented by a solid line connecting sites $i(b)$ and $j(b)$. Obviously the rule for writing down the contribution of a simple diagram is to take a factor $(-\beta J)^m/m!$ for each bond

covered by m solid lines and to multiply the result by the cumulant average required in Eq. (3.5). Figure 9 contains a number of simple diagrams which arise in the calculation for $m\leq 4$. It is instructive to calculate the expansion for n-component classical unit vector spins, including not only the Ising, XY, and Heisenberg models $(n=1,2$ and 3) but also the self-avoiding walk problem for which[32] $n=0$. To generalize the results of this section to spins of length S, one should replace J by JS^2, or better (to take partial account of quantum effects) by $JS(S+1)$.

Thus the diagram for $m=1$ in Fig. 9 represents

$$-\beta J\langle(\mathbf{S}_i\cdot\mathbf{S}_j)^2\rangle_c=-\beta J\langle(S_j^z)^2\rangle_0=-(\beta J/n)\ .\tag{3.6}$$

Note that this diagram only occurs when i and j are nearest neighbors. For $m = 2$, the diagram in parentheses is zero because there are an odd number of spin operators at each site. In general for these classical models any diagram with an odd number of bonds ending at a site (including the external bond) is zero. Thus the only nonzero contributions of order β^2 come from the second $m = 2$ diagram in Fig. 9,

$$(\beta J)^2 \langle (\mathbf{S}_i \cdot \mathbf{S}_j)(\mathbf{S}_j \cdot \mathbf{S}_k)(\mathbf{S}_k \cdot \mathbf{S}_i) \rangle_c = (\beta J / n)^2 . \tag{3.7}$$

For this diagram, i and j can be first, second, or third neighbors and each occurs only once for a given (i, j) pair.

In order β^3, if i and j are nearest neighbors, there is a contribution corresponding to the first $m = 3$ diagram,

$$[(-\beta J)^3/3!]\langle \mathbf{S}_i \cdot \mathbf{S}_j)^4 \rangle_c = [(-\beta J)^3/3!]$$

$$\times [\langle (\mathbf{S}_i \cdot \mathbf{S}_j)^4 \rangle_0 - 3\langle (\mathbf{S}_i \cdot \mathbf{S}_j)^2 \rangle_0]$$

$$= (\beta J / n)^3 n /(n +2) . \tag{3.8}$$

The second diagram (in parentheses) for $m = 3$ is zero because of the cumulant property. In general, any diagram which can be separated into two parts by deleting a single site has zero cumulant. The last diagram for $m = 3$ in Fig. 9 is nonzero for pairs of sites which can be reached in three nonretracting steps. Its value is

$$(-\beta J)^3 \langle (\mathbf{S}_i \cdot \mathbf{S}_j)(\mathbf{S}_j \cdot \mathbf{S}_k)(\mathbf{S}_k \cdot \mathbf{S}_l)(\mathbf{S}_l \cdot \mathbf{S}_i) \rangle_0 = -(\beta J / n)^3 . \tag{3.9}$$

If sites i and j can be connected by k 3-step self-avoiding walks, then the contribution in Eq. (3.9) must be counted

k times.

So, up to order $(\beta J)^3$ we have (dropping the subscript β on thermal averages)

$$\langle \mathbf{S}_0 \cdot \mathbf{S}_1 \rangle = -y + y^2 + ny^3/(n +2) , \tag{3.10a}$$

$$\langle \mathbf{S}_0 \cdot \mathbf{S}_2 \rangle = 2\langle \mathbf{S}_0 \cdot \mathbf{S}_7 \rangle = 2\langle \mathbf{S}_0 \cdot \mathbf{S}_5 \rangle = 2\langle \mathbf{S}_0 \cdot \mathbf{S}_8 \rangle = -2y^3 , \tag{3.10b}$$

$$\langle \mathbf{S}_0 \cdot \mathbf{S}_3 \rangle = \langle \mathbf{S}_0 \cdot \mathbf{S}_4 \rangle = y^2 - 2y^3 , \tag{3.10c}$$

where $y = \beta J / n$, and the sites are labeled as in Fig. 10.

For larger values of m, the number of diagrams increases rapidly, and it becomes necessary to organize the various terms in the sum in a more economical fashion. It is convenient to combine all simple diagrams which involve the same bonds, but differ only by the number of multiple coverings of bonds. We therefore introduce "dressed" diagrams which correspond to summing over all coverings $m_i = 1, 2, 3, \ldots$, of the ith bond. Obviously, if we work to a fixed order, say mth, in (βJ), then for any diagram we only need sum over simple diagrams having $\sum_i m_i \le m$. Introduction of this shorthand does not shorten the calculation except insofar as it makes it easier to keep track of the various terms. As was the case for simple diagrams, the cumulant average vanishes for all diagrams with an articulation point, i.e., a point which, if removed, causes the diagram to become disconnected with respect to solid or dashed lines. Thus chain diagrams contribute only if the external line connects the two ends of the chain. Furthermore, the contribution from a given diagram depends only on its topology (connectivity) and not on its exact shape. Thus all diagrams consisting of chains of a given length in which the external line connects the ends of the chain give identical contributions to the end-to-end correlation function irrespective of their
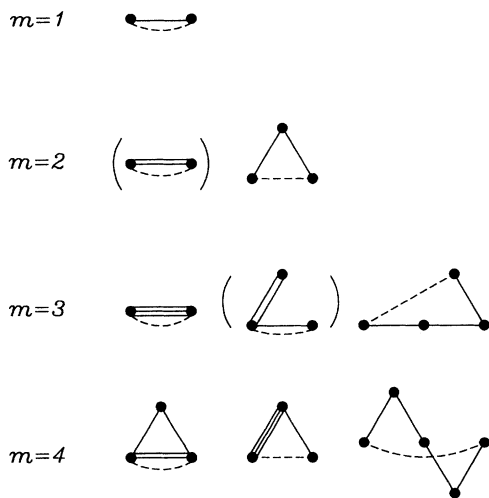

FIG. 9. "Simple" diagrams of low-order m which contribute to the cumulant expansion of Eq. (3.5). Solid lines represent interactions in the Hamiltonian. Dashed lines are "external" lines corresponding to the operator, $\mathbf{S}_i \cdot \mathbf{S}_j$. For a classical model, such as treated here, diagrams with an odd number of lines emanating from any vertex give zero contribution, e.g., the diagram in parentheses for $m = 2$. The diagram in parentheses for $m = 3$ vanishes when the cumulant average is taken. Other diagrams which give zero contribution are omitted.
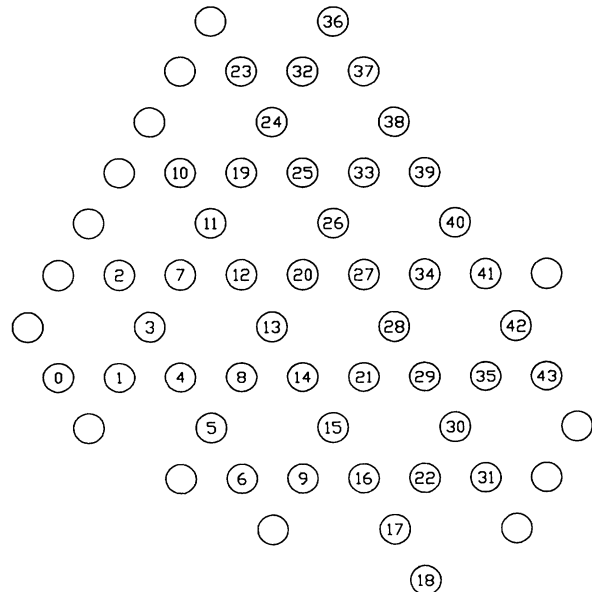

FIG. 10. Sites (numbered 1 through 43) in one quadrant of the lattice which can be reached from the origin in eight steps or less.

exact shape. For the present calculation, extending to $m = 8$, there are 23 topology classes of diagrams, each involving 8 or fewer bonds with the external bonds explicitly labeled. The diagrams for these topology classes (labeled 1a through 8b, where the number refers to the number of bonds) are shown in Fig. 11. Since the solid lines in Fig. 11 represent one or more factors $S_{i(b)} \cdot S_{j(b)}$ from the Hamiltonian, a diagram with m solid lines can only contribute in order β^m and/or higher. For example, 1a contributes terms of order β^{2j+1}, $j = 0, 1, 2, \ldots$, whereas diagrams 8a and 8b contribute in order β^8 and higher. Thus each diagram d with m bonds gives rise to a contribution to $\langle S_i \cdot S_j \rangle$ of the form

$$\langle S_i \cdot S_j \rangle = \sum_{l \geq m} C_d^l y^l . \tag{3.11}$$

The evaluation of diagrams with m up to 8 is given in Appendix B along with a number of useful identities. The results of all diagrams are presented in Appendix B in terms of quantities C_d^l. Our aim, of course, is to calculate $\langle S(r_\alpha) \cdot S(R + r_\beta) \rangle$. To get this correlation function we must combine the C_d^l with the statistics of the positions of the sites linked by the external line. In other words, the correlation functions $\langle S(r_\alpha) \cdot S(R + r_\beta) \rangle$ are given by the cumulant averages C_d^l, defined above, times
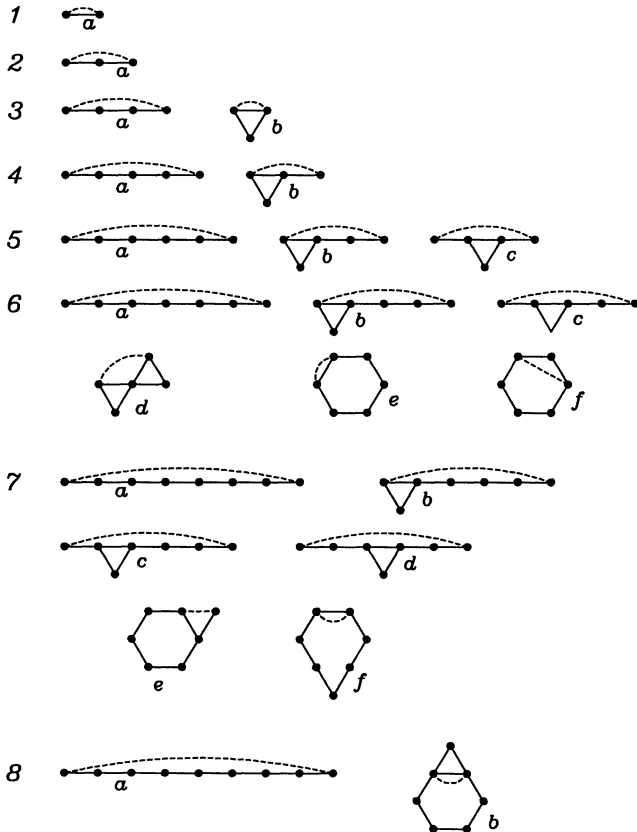

FIG. 11. Twenty-three "topology classes" of "dressed" diagrams used to calculate the coefficients C_d^l which appear in Eq. (3.10) and whose values are listed in Appendix B. The dashed lines are "external" lines.

a factor $N_d(R + r_\beta - r_\alpha)$, which is the number of different diagrams having topology d which connect the site at r_α to the site at $R + r_\beta$. For example, diagram 1a connects sites 0 and 1 in Fig. 10 only once, whereas there are 30 ways that these sites are connected by diagram 8a. Accordingly, we write

$$\langle S(r_\alpha) \cdot S(R + r_\beta) \rangle = \sum_d N_d(R)_{\alpha,\beta} \sum_l C_d^l y^l . \tag{3.12}$$

In view of the symmetry of the lattice it suffices to tabulate $N_d(R)_{\alpha,\beta}$ for a single value of α, which we may designate as the origin. In Fig. 10 the sites in one quadrant of the lattice which can be reached in eight or less steps from the origin are numbered 1 to 43. Data for $N_d(R)_{1,\beta}$ for such sites are given in Table I. Data for sites in the other quadrants can be obtained using the mirror-plane symmetry with respect to the planes bounding the quadrant of numbered sites shown in Fig. 10. The wave-vector-dependent susceptibility $\chi_{\alpha\beta}(q)$ is given by

$$\chi_{\alpha\beta}(q) = \langle S_\alpha(q) \cdot S_\beta(-q) \rangle , \tag{3.13}$$

where

$$S_\alpha(q) = \frac{1}{\sqrt{N}} \sum_R S(R + r_\alpha) e^{iq \cdot (R_i + r_\alpha)} . \tag{3.14}$$

Since we are dealing with a classical model, the wave-vector-dependent susceptibility $\chi(q)$ and the correlation function at that wave vector differ only by a factor of T, which we ignore in this section. In the next section, when we make comparison with experiment, we will distinguish between these quantities. Thus

$$\chi_{\alpha\beta}(q) = \sum_R \langle S(r_\alpha) \cdot S(R + r_\beta) \rangle e^{-iq \cdot (R + r_\beta - r_\alpha)} . \tag{3.15}$$

The susceptibility defined in Eq. (3.15) is a 3×3 matrix for each value of q in the Brillouin zone. The eigenvectors of this matrix are "normal modes" of the disordered spin system which can be induced independently by the appropriate wave-vector-dependent field. The corresponding eigenvalues are the susceptibilities of these modes. To first order in $y = \beta J / n$ the susceptibility is

$$\chi(q) = \begin{bmatrix} 1 & -2y \cos q \cdot r_{21} & -2y \cos q \cdot r_{31} \\ -2y \cos q \cdot r_{21} & 1 & -2y \cos q \cdot r_{32} \\ -2y \cos q \cdot r_{31} & -2y \cos q \cdot r_{32} & 1 \end{bmatrix} . \tag{3.16}$$

The largest eigenvalue of this matrix is $\chi_1 = (1 + 2y)$ for which the eigenvector is $\hat{v}_1$ of Eq. (2.14).

In order y^2 the susceptibility picks up Fourier components involving second and third neighbors with equal amplitudes. For this case, we find that $\hat{v}_1$ is still an eigenvector, as it was for the case $J_2 = J_3$ in the linear-spin-wave calculation of Sec. II, and $\chi_1 = (1 + 2y)$ to order y^2. In fact, we find that the largest eigenvalue of the susceptibility is independent of q and its eigenvector remains identical to v_1 through order y^7.

To see how this happens in more detail we write v_1 as

$$v_{1\alpha} = \sin\mathbf{q}\cdot\mathbf{r}_{\beta\gamma} ,$$

(3.17)

$$\chi_{\alpha\beta}(\mathbf{q}) = \sum_R \chi_{\alpha\beta}(\mathbf{R})\cos\mathbf{q}\cdot(\mathbf{R}+\mathbf{r}_{\alpha\beta}) .$$

(3.18)

where $\mathbf{r}_{\beta\gamma} = \mathbf{r}_\beta - \mathbf{r}_\gamma$, $(\alpha,\beta,\gamma) = (1,2,3)$ cyclically permutated, and

If $\mathbf{v}_1$ is an eigenvector, then

$$\sum_R [\chi_{31}(\mathbf{R})\cos\mathbf{q}\cdot(\mathbf{R}+\mathbf{r}_{13})\sin\mathbf{q}\cdot\mathbf{r}_{23} + \chi_{32}(\mathbf{R})\cos\mathbf{q}\cdot(\mathbf{R}+\mathbf{r}_{23})\sin\mathbf{q}\cdot\mathbf{r}_{31} + \chi_{33}(\mathbf{R})\cos\mathbf{q}\cdot\mathbf{R}\sin\mathbf{q}\cdot\mathbf{r}_{12}] = \chi_1\sin\mathbf{q}\cdot\mathbf{r}_{12} ,$$

(3.19a)

which gives

$$\frac{1}{2}\sum_R [\chi_{31}(\mathbf{R})\sin\mathbf{q}\cdot(\mathbf{r}_{23}+\mathbf{R}+\mathbf{r}_{13}) + \chi_{31}(\mathbf{R})\sin\mathbf{q}\cdot(\mathbf{r}_{21}-\mathbf{R}) + \chi_{32}(\mathbf{R})\sin\mathbf{q}\cdot(\mathbf{r}_{21}+\mathbf{R}) + \chi_{32}(\mathbf{R})\sin\mathbf{q}\cdot(\mathbf{r}_{31}-\mathbf{r}_{23}-\mathbf{R})$$

$$+ \chi_{33}(\mathbf{R})\sin\mathbf{q}\cdot(\mathbf{r}_{12}+\mathbf{R}) + \chi_{33}(\mathbf{R})\sin\mathbf{q}\cdot(\mathbf{r}_{12}-\mathbf{R})] = \chi_1\sin\mathbf{q}\cdot\mathbf{r}_{12} .$$

(3.19b)

TABLE I. Values of $N_d(\mathbf{R})_{\alpha,\beta}$. As explained in the text, we take one site to be at the origin and the other site is at a position labeled s, according to Fig. 10.

$d=$	1a	2a	3a	4a	3b	4b	5b	6b	5c	6c	6e	6f	7f	7e	6d	8b
s																
1	1	1	0	0	1	0	0	0	0	0	1	0	7	2	0	1
2	0	0	2	6	0	0	4	8	2	4	0	0	0	0	0	0
3	0	1	2	2	0	2	2	2	0	2	0	1	0	0	1	0
4	0	1	2	1	0	2	2	0	0	0	0	0	0	2	1	0
5	0	0	1	4	0	0	2	6	1	4	0	0	0	0	0	0
6	0	0	0	2	0	0	0	4	0	4	0	0	0	0	0	0
7	0	0	1	4	0	0	2	6	1	4	0	0	0	0	0	0
8	0	0	1	3	0	0	2	4	1	2	0	0	0	0	0	0
9	0	0	0	0	0	0	0	0	0	0	0	0	0	0	0	0
10	0	0	0	0	0	0	0	0	0	0	0	0	0	0	0	0
11	0	0	0	1	0	0	0	2	0	2	0	0	0	0	0	0
12	0	0	0	1	0	0	0	2	0	2	0	0	0	0	0	0
13	0	0	0	1	0	0	0	2	0	2	0	0	0	0	0	0
14	0	0	0	1	0	0	0	2	0	2	0	0	0	0	0	0

$s=$	1	2	3	4	5	6	7	8	9	10	11	12	13	14	15
d															
5a	1	6	4	2	7	8	7	4	2	2	5	6	5	4	1
6a	7	2	7	10	8	12	8	8	11	12	13	16	13	8	7
7a	20	4	12	22	12	12	12	23	27	34	27	26	27	20	24
8a	30	32	30	34	35	32	35	51	46	64	51	38	51	59	57
7b	2	4	6	4	8	12	8	4	4	4	8	10	8	6	2
7d	1	2	2	2	3	4	3	2	2	2	3	4	3	2	1
7c	2	0	4	4	4	8	4	2	4	4	6	8	6	4	1

$s=$	16	17	18	19	20	21	22	23	24	25	26	27	28	29	30
d															
5a	0	0	0	1	2	1	0	0	0	0	0	0	0	0	0
6a	3	0	0	7	11	5	0	0	1	1	2	2	1	1	0
7a	18	3	0	24	27	14	3	2	8	10	14	14	8	6	1
8a	48	24	6	57	46	42	22	18	34	46	48	46	34	21	10
7b	0	0	0	2	4	2	0	0	0	0	0	0	0	0	0
7d	0	0	0	1	2	1	0	0	0	0	0	0	0	0	0
7c	0	0	0	2	4	4	0	0	0	0	0	0	0	0	0

$s=$	31	32	33	34	35	36	37	38	39	40	41	42	43
d													
7a	0	1	3	3	1								
8a	4	10	24	22	7	1	1	3	3	3	3	1	1

The left-hand side of this equation can be written as a Fourier series so that

$$\sum_{\mathbf{R}} M(\mathbf{R})\sin\mathbf{q}\cdot(\mathbf{R}+\mathbf{r}_{12})=\chi_1\sin\mathbf{q}\cdot\mathbf{r}_{12} \ , \tag{3.20}$$

with

$$M(\mathbf{R})=\tfrac{1}{2}[\chi_{31}(\mathbf{R}-2\mathbf{r}_{23})-\chi_{31}(\mathbf{R})+\chi_{32}(\mathbf{R}+2\mathbf{r}_{12})-\chi_{32}(\mathbf{R}+2\mathbf{r}_{32})+\chi_{33}(\mathbf{R})-\chi_{33}(\mathbf{R}+2\mathbf{r}_{12})] \ . \tag{3.21}$$

Equation (3.20) gives

$$M(\mathbf{R})-M(-\mathbf{R}-2\mathbf{r}_{12})=\chi_1\delta_{\mathbf{R},0} \ . \tag{3.22}$$

As we shall see, the sum in Eq. (3.21) may be identified with a sum around a hexagon of sites. To facilitate this identification we set $\mathbf{R}_H\equiv\mathbf{R}+\mathbf{r}_{12}$. Then if we set $\chi_{3,\alpha}(\mathbf{R})=\chi(\mathbf{R}+\mathbf{r}_\alpha)$, we have

$$M(\mathbf{R})=\tfrac{1}{2}[\chi(\mathbf{R}_H-\mathbf{r}_{23})-\chi(\mathbf{R}_H+\mathbf{r}_{23})+\chi(\mathbf{R}_H+\mathbf{r}_{13})$$

$$-\chi(\mathbf{R}_H-\mathbf{r}_{13})+\chi(\mathbf{R}_H+\mathbf{r}_{21})-\chi(\mathbf{R}_H-\mathbf{r}_{21})]$$

$$\equiv \hat{M}(\mathbf{R}_H) \ , \tag{3.23}$$

where $\mathbf{R}_H$ is the location of the center of the hexagon relative to the origin (which is on sublattice 3). Using this representation it is easy to show that

$$M(-\mathbf{R}-2\mathbf{r}_{12})=-M(\mathbf{R}) \ , \tag{3.24}$$

so that Eq. (3.22) is

$$2M(\mathbf{R})=\chi_1\delta_{\mathbf{R},0} \ . \tag{3.25}$$

Referring to Fig. 5, one sees that $M(\mathbf{R})$ represents a sum over a hexagon of sites centered at $\mathbf{R}_H$ with alternating signs, just as in Eq. (2.26).

Let us now see if our assumption about $\mathbf{v}_1$ being an eigenvector associated with a dispersionless eigenvalue is correct. First of all, the eigenvalue χ_1, given in Eq. (3.25), is indeed independent of $\mathbf{q}$. Its value is related to the sum around a hexagon which includes the origin. In Fig. 12 the two hexagons of this type (which are equivalent by symmetry) are labeled "χ_1." For values of $\mathbf{R}\neq0$, Eq. (3.25) indicates that the sum over any hexagon vanishes. In other words, the condition that the eigenvalue χ_1 be independent of $\mathbf{q}$ is that the sum in Eq. (3.23) vanish when taken over any hexagon which does not include the

origin.

The two hexagons closest to the site at the origin which do not include the origin are centered at $\pm(\mathbf{r}_1+\mathbf{r}_2)$. For these hexagons, labeled "0" in Fig. 12, Eq. (3.25) is satisfied identically by symmetry. The next closest hexagons are labeled A_i in Fig. 12. We find that, for these hexagons, Eq. (3.25) is first violated in eighth order in the high-temperature expansion. Presumably more distinct hexagons show violations of Eq. (3.25) in still higher order in (βJ). Thus in eighth order, all of the eigenvalues of $\chi_{\alpha\beta}(\mathbf{q})$ have dispersion.[34]

We now develop an expression for the dispersion in the largest eigenvalue $\chi_1(\beta J,\mathbf{q})$. For this purpose we write above the results as

$$\sum_\alpha \chi_{3\alpha}(\mathbf{q})v_{1\alpha}(\mathbf{q})=\sum_H \hat{M}(\mathbf{R}_H)\sin(\mathbf{q}\cdot\mathbf{R}_H) \ , \tag{3.26a}$$

where $\hat{M}(\mathbf{R}_H)$ is as defined in Eq. (3.23). Similarly we find that

$$\sum_\alpha \chi_{1\alpha}(\mathbf{q})v_{1\alpha}(\mathbf{q})=-\sum_H \hat{M}(\mathbf{R}_H)\sin[(\sigma_{\pi/2}\mathbf{q})\cdot\mathbf{R}_H] \ , \tag{3.26b}$$

$$\sum_\alpha \chi_{2\alpha}(\mathbf{q})v_{1\alpha}(\mathbf{q})=-\sum_H \hat{M}(\mathbf{R}_H)\sin[(\sigma_{\pi/3}\mathbf{q})\cdot\mathbf{R}_H] \ , \tag{3.26c}$$

where σ_ϕ is a reflection about the line $y\cos\phi-x\sin\phi=0$. [Thus if $\mathbf{q}=(q_x,q_y)$, then $\sigma_{\pi/2}\mathbf{q}=(-q_x,q_y)$.] If we write $\chi=\chi_0+V$, where V is the contribution to χ which causes dispersion in $\chi_1(\mathbf{q})$, we see that V is of order $(\beta J)^8$. That means that first-order perturbation theory in V is accurate up to order $(\beta J)^{15}$. Thus

$$\chi_1(\beta J,\mathbf{q})=\frac{\sum_{\alpha\beta}v_{1\alpha}(\mathbf{q})\chi_{\alpha\beta}(\beta J,\mathbf{q})v_{1\beta}(\mathbf{q})}{\sum_\alpha[v_{1\alpha}(\mathbf{q})]^2}+O((\beta J)^{16}) \ . \tag{3.27}$$

Thus

$$\chi_1(\beta J,\mathbf{q})=\sum_H \hat{M}(\mathbf{R}_H)\left[\frac{\sin\mathbf{q}\cdot\mathbf{r}_{12}\sin\mathbf{q}\cdot\mathbf{R}_H-\sin\mathbf{q}\cdot\mathbf{r}_{23}\sin\sigma_{\pi/2}\mathbf{q}\cdot\mathbf{R}_H-\sin\mathbf{q}\cdot\mathbf{r}_{31}\sin\sigma_{\pi/3}\mathbf{q}\cdot\mathbf{R}_H}{\sin^2\mathbf{q}\cdot\mathbf{r}_{12}+\sin^2\mathbf{q}\cdot\mathbf{r}_{23}+\sin^2\mathbf{q}\cdot\mathbf{r}_{31}}\right] \ . \tag{3.28}$$

When $\hat{M}(\mathbf{R}_H)$ is zero except for $\mathbf{R}_H=\pm\mathbf{r}_{12}$, the factor in large parentheses is unity, yielding the correct q-independent result for χ_1. To order $(\beta J)^8$,

$$\chi_1(\beta J,\mathbf{q})=2\hat{M}(\mathbf{r}_{12})+2\hat{M}(\mathbf{R}_{A_2})F_A(\mathbf{q}) \ , \tag{3.29}$$

where $\mathbf{R}_{A_2}$ is the position of the center of hexagon A_2 in Fig. 12. From Figs. 10 and 12 we have

$$\hat{M}(\mathbf{R}_{A_2})=\langle \mathbf{S}_0\cdot(\mathbf{S}_4+\mathbf{S}_7+\mathbf{S}_{13}-\mathbf{S}_3-\mathbf{S}_8-\mathbf{S}_{12})\rangle \ , \tag{3.30}$$

and using Table I and Appendix B we get

$$\hat{M}(\mathbf{R}_{A_2}) = -\frac{4(n-1)y^8}{(n+2)^2} + O(y^9) \ . \tag{3.31}$$

We construct $F_A(\mathbf{q})$ as

$$F_A(\mathbf{q}) = \left[\sin\left[\frac{q_x}{2} + \frac{\sqrt{3}q_y}{2}\right] \sin\left[\frac{5q_x}{2} + \frac{\sqrt{3}q_y}{2}\right] - \sin\left[\frac{q_x}{2} + \frac{\sqrt{3}q_y}{2}\right] \sin\left[\frac{q_x}{2} - \frac{3\sqrt{3}q_y}{2}\right] \right.$$

$$- \sin\left[\frac{q_x}{2} - \frac{\sqrt{3}q_y}{2}\right] \sin\left[-\frac{5q_x}{2} + \frac{\sqrt{3}q_y}{2}\right] - \sin\left[\frac{q_x}{2} - \frac{\sqrt{3}q_y}{2}\right] \sin\left[\frac{q_x}{2} + \frac{3\sqrt{q_y}}{2}\right]$$

$$\left. + \sin(q_x)\sin(2q_x + \sqrt{3}q_y) - \sin(q_x)\sin(-2q_x + \sqrt{3}q_y) \right] \bigg/ (\sin^2\mathbf{q}\cdot\mathbf{r}_{12} + \sin^2\mathbf{q}\cdot\mathbf{r}_{23} + \sin^2\mathbf{q}\cdot\mathbf{r}_{31}) \ . \tag{3.32}$$

From Eq. (3.31) we see that the dispersion of the largest eigenvalue is proportional to $n-1$. The extrema of χ_1 occur at $\mathbf{q}=0$ where $F_A(0)=4$ and at $\mathbf{q}=\mathbf{q}_{\sqrt{3}}$ where $F_A(\mathbf{q}_{\sqrt{3}}) = -2$. That is, the maximum susceptibility is at $\mathbf{q}=0$ for $n=0$ (the self-avoiding walk); the band is flat for the Ising case $(n=1)$; and the maximum is at $\mathbf{q}=(\pm 2\pi/3,0)$ for the XY $(n=2)$ and Heisenberg $(n=3)$ cases. Thus the degeneracy is not removed for the Ising model in this order, and there is a slight tendency toward $\sqrt{3}\times\sqrt{3}$ ordering for the classical nearest-neighbor XY and Heisenberg antiferromagnetic on a kagomé lattice. However, this tendency could easily be overwhelmed by further neighbor interactions and/or quantum effects.

These conclusions are physically reasonable. First of all, the self-avoiding-walk correlation function should decrease monotonically with distance. That is, it should show no tendency to form sublattices. For magnetic problems, in particular for the Heisenberg model, the sit-

uation is quite different. For the classical model, the ground-state energies of the two structures shown in Fig. 3 are identical. However, as we have said, the $\sqrt{3}\times\sqrt{3}$ structure has a nonzero entropy per site, whereas the other structure has zero entropy per site at $T=0$. Thus, at finite temperature, and in particular within the high-temperature expansion, we might expect the $\sqrt{3}\times\sqrt{3}$ structure to have a lower free energy. This result is indicated by the fact that the high-temperature susceptibility is maximal at the wave vector appropriate to the $\sqrt{3}\times\sqrt{3}$ structure.

Some numerical results for the high-temperature expansion of $\chi_{\alpha\beta}(\mathbf{q})$ for $n=3$ are presented in Fig. 13 which shows the three eigenvalues of $\chi_{\alpha\beta}(\mathbf{q})$ plotted versus $\mathbf{q}$ for $\beta J=0.9$. Note that the twofold degeneracy at $\mathbf{q}=0$ is an exact symmetry of the lattice.

We have also performed a high-temperature expansion of the susceptibility for the $n=0$ model on a 3D pyrochlore structure and obtained essentially the same results as for the kagomé. That is, we find that the largest eigenvalues of the susceptibility are dispersionless to order β^7 and that a $\mathbf{q}=0$ mode is favored for $n=0$ (self-avoiding walks) in order β^8. As for the kagomé, the condition for dispersionless modes (two degenerate modes per $\mathbf{q}$ vector for pyrochlore) can be expressed in terms of susceptibilities summing to zero around hexagons, which here do not lie in a single plane, however. Presumably for the
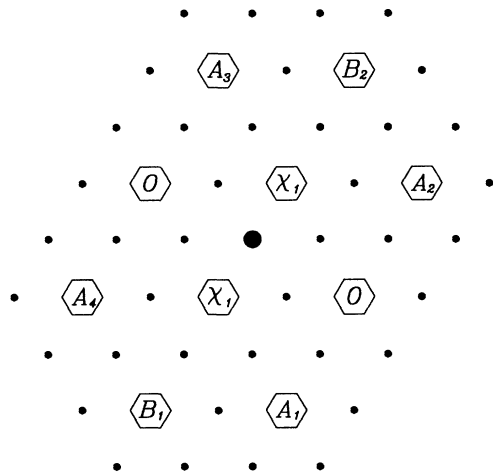

FIG. 12. The hexagons of sites on the right-hand side of Eqs. (3.23) and which are thus involved in Eq. (3.25). The large dot represents the origin. Smaller dots are kagomé lattice points. Each hexagon of sites is indicated by a hexagon at its center, inside of which is given an identifying label for that hexagon, to facilitate the discussion in the text. All the hexagons with "A" labels (or "B", or "χ" labels) are equivalent to one another by symmetry.
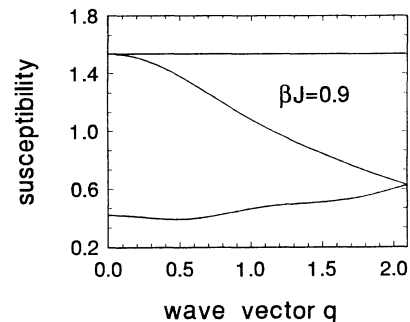

FIG. 13. Eigenvalues of the wave-vector-dependent susceptibility $\chi_{\alpha\beta}(\mathbf{q})$ obtained from the eighth-order high-temperature expansion for $\beta J=0.90$ plotted vs $\mathbf{q}=(q,0)$. The dispersion of the highest mode is given by Eq. (3.29) in the text.

Heisenberg model ($n=3$) a wave vector on the zone boundary will be favored.

IV. COMPARISON TO EXPERIMENT: $\chi_0(T)$ AND $I(q,T)$

The high-temperature expansion of $\chi_{\alpha\beta}(\mathbf{q})$ derived above can be compared to experimental data on the uniform, static susceptibility $\chi_0(T)$ of kagomé systems[27–29,35] and to powder-neutron-diffraction data.[28] We work in units such that $\chi_0(T)$ may be written as

$$\chi_0(T)=\frac{1}{T}\sum_r \langle \mathbf{S}_0\cdot\mathbf{S}_r \rangle \ . \tag{4.1}$$

Using the results of Sec. III and Appendix B we obtain

$$T\chi_0(T)=\sum_{m=0}^{8} a_m y^m \ , \tag{4.2}$$

where

$$a_0=1, \ a=-4, \ a_2=12, \ a_3=-29.6, \ a_4=66.4 \ , \tag{4.3}$$

$$a_5=-\frac{256\,44}{175}, a_6=\frac{560\,68}{175}, a_7=\frac{131\,584}{175}, a_8=\frac{809\,928\,4}{6125} .$$

As noted above, to treat spins of length S we replace J by $\tilde{J}\equiv JS(S+1)$. Thus for the most appropriate identification with experiment we set $y=\beta JS(S+1)/n=\tilde{J}/(nT)$. Although Eq. (4.2) can be applied directly, a more efficient use of the information contained in the expansion coefficients is obtained by constructing Padé approximants[36] of the form

$$P_{M,N}(y)=\frac{1+b_1 y+\cdots+b_M y^M}{1+c_1 y+\cdots+c_N y^N} \ . \tag{4.4}$$

In particular we have constructed the diagonal Padé approximants $P_{M,M}$ to $\chi_0(T)$ for $M=1,2,3,4$. The results are plotted in the form $1/\tilde{J}\chi_0(T)$ versus $T/\tilde{J}$ in Fig. 14. The curves in Fig. 14 give some indication of how rapidly the sequence is converging. They suggest that the [4,4] Padé should be accurate to within a few percent down to $T/\tilde{J}=\frac{1}{2}$. This function provides a useful way of fitting the experimental data of Aeppli et al.[35] for $T/\tilde{J}>\frac{1}{2}$, and
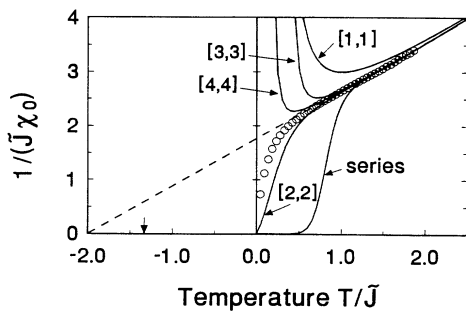

FIG. 14. Comparison of experimental (circles) and theoretical (solid lines) values of the inverse uniform susceptibility, $1/\chi(\mathbf{q}=0)$, plotted vs temperature. The curve marked "series" is the result from the eight-term series for $\chi(\mathbf{q}=0)$. The vertical arrow on the negative temperature axis is at $T/\tilde{J}=-\frac{4}{3}$. See the text for a discussion of the negative temperature intercepts.

of extracting the parameter $\tilde{J}$.

The value of $\tilde{J}$ is obtained by noting that the experimental data for $SrCr_{8-x}Ga_{4+x}O_{19}$ containing spin-$\frac{3}{2}$ Cr atoms, extrapolate to zero at -430 K and that the data fall in the range $0<T<400$ K. By comparison, if we examine the theoretical curves for $0<T/\tilde{J}<2$, we find that a straight line through the higher-temperature points extrapolates to zero at $T/\tilde{J}\approx-2$, yielding $\tilde{J}\approx215$ K, i.e., $J\approx57$ K for $S=\frac{3}{2}$. Note that JS is the scale factor for the spin-wave frequencies calculated in Sec. II. The normalization of χ_0 is fixed by fitting the data to the theoretical curves at $T/\tilde{J}=1$. The data, thus scaled, are shown by the open circles in Fig. 14. We note that, although the data appear to follow a Curie-Weiss law, they do not in fact extend to the high-temperature regime $\tilde{J}/T\ll1$. The Curie-Weiss function which coincides with the high-temperature behavior of our expansion is

$$\chi_0=\frac{1}{T+4\tilde{J}/3} \ , \tag{4.5}$$

which intercepts the horizontal axis of Fig. 14 at $T/\tilde{J}=-\frac{4}{3}$, not at $T/\tilde{J}=-2$. Also the high-temperature limiting slope of $1/(\tilde{J}\chi_0)$ is equal to 1 rather than to the value of about $\frac{8}{9}$ shown in the figure.

The comparison of the sequence of Padés, shown in Fig. 14, to the data suggests that a higher-order expansion would extend the linear temperature dependence of $1/(\tilde{J}\chi_0)$ to even lower temperature. It is tempting to speculate about whether the exact theoretical result would exhibit the low-temperature drop seen in the data. We expect that it would not and that the low-temperature behavior of the experimental data results from the fact that, in the experimental system, $SrCr_{8-x}Ga_{4+x}O_{19}$ the spin-$\frac{3}{2}$ Cr atoms which lie in the kagomé layers are diluted with spinless Ga atoms, even for $x=0$.[27] In the experiments of Aeppli and co-workers[35] ($x=0.87$), the concentration of Cr in the kagomé layers was about 80%. As a general rule, dilution with nonmagnetic atoms relieves frustration. For the kagomé system even a small amount of dilution will also act to lift the degeneracy of the ground state, yielding a stable spin-glass-like state as is observed experimentally.[28,35]

Powder-neutron diffraction measures the angular average of the equal-time correlation function $\sum_{\alpha,\beta}\chi_{\alpha\beta}(\mathbf{q})$,

$$I(q,T)=\left\langle\frac{1}{3}\sum_{\alpha,\beta}\chi_{\alpha\beta}(\mathbf{q})\right\rangle_{powder} , \tag{4.6}$$

where the powder average is over all directions of $\mathbf{q}$ on the unit sphere. The high-temperature expansion for $I(q,T)$ is effected by replacing every factor of the form $\cos\mathbf{q}\cdot\mathbf{r}$ in $\chi_{\alpha\beta}$ with $\sin(qr)/(qr)$. The curve $I(q,T)$ versus q, Fig. 15, exhibits a broad peak near $Q_0=4\pi/3a$ in agreement with the results of Broholm et al.[28] We note that the presence of a peak at Q_0 says nothing about whether the order is of the $\mathbf{q}=0$ or $\sqrt{3}\times\sqrt{3}$ type. It simply reflects the short-range antiferromagnetic order on the kagomé lattice. Our theoretical intensity, derived from equal time correlation functions, corresponds to experimental data integrated up to energies much larger
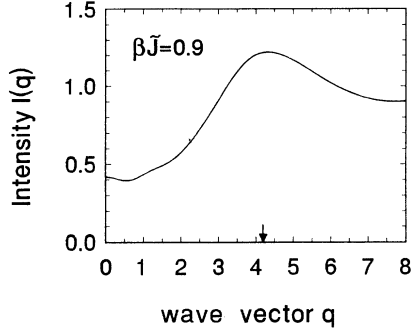
FIG. 15. Powder-diffraction cross section, $I(q)$ (integrated over all energy transfers), for $\beta\tilde{J}=0.9$, as a function of momentum transfer, q. The arrow indicates the value of $Q_0=4\pi/3$. The nearest-neighbor distance a has been set equal to 1.

than $\tilde{J}$, whereas the data of Ref. 28 are for energies less than 5 meV or about a quarter of $\tilde{J}$. Nevertheless, the shape of the experimental diffraction peak at low temperature ($T=1.5$ K) is quite similar to our high-temperature result evaluated at $\beta\tilde{J}=0.9$. Thus it appears that our expansion to order $(\beta J)^8$ captures at least the qualitative features of the short-range order observed at low temperature in this system.

V. CONCLUSIONS

In this paper we have studied the Heisenberg model on a kagomé lattice using linearized spin-wave theory and a high-temperature expansion for the two-point correlation function. Spin-wave theory was carried out for antiferromagnetic nearest-neighbor interactions, $J_1>0$ and nonzero second- and third-neighbor interactions, J_2 and J_3, and for the two structures which we called q=0 [Fig. 3(a)] and $\sqrt{3}\times\sqrt{3}$ [Fig. 3(b)]. The high-temperature expansion of the spin-spin correlation function $\chi_{\alpha\beta}$, where α and β label the three sublattices of the kagomé lattice, was developed for arbitrary n-component classical models with only nearest-neighbor interactions, up to eighth order in (J_1/kT). χ_1, the maximum eigenvalue of $\chi_{\alpha\beta}$, was obtained by diagonalizing $\chi_{\alpha\beta}$. From this work our conclusions are as follows.

(1) The spin-wave calculations indicate that, for small J_2 and J_3, the $\sqrt{3}\times\sqrt{3}$ state is favored for $J_2<J_3$ and the q=0 state is favored for $J_2>J_3$. Since we only considered these two candidates for spin ordering, we cannot guarantee these states to be absolute ground states.

(2) For either structure, the spin-wave velocity of the lowest-energy mode is proportional to $\sqrt{|J_2-J_3|}$. Experimentally one might expect J_2 and J_3 to be comparable in magnitude, and hence that J_2-J_3 could have either sign. For either case, the temperature scale for the development of order will be much smaller than J_1 and possibly also significantly smaller than J_2, if J_2-J_3 is smaller in magnitude than J_2.

(3) For the $\sqrt{3}\times\sqrt{3}$ structure there is a low-lying optical mode with energy $3S[(2J_1-4J_2)(J_3-J_2)]^{1/2}$ in addition to the optical mode near energy $2J_1S$. The q=0 structure has no optical modes. Both structures will exhibit two magnon Raman scattering with anomalously

large strength at low frequencies because of the large density of excitations due to the mode whose frequency is zero in the classical model when $J_2=J_3$. Similarly the nuclear spin lattice relaxation rate is expected to be anomalously large in these systems.

(4) The high-temperature expansion shows that the degeneracy found in mean-field theory,[17] that $\chi_1(\mathbf{q})$ is $\mathbf{q}$ independent for the nearest-neighbor model, is not exact. This removal of degeneracy was also demonstrated for the pyrochlore lattice which may be viewed as a generalization of the kagomé lattice to three dimensions.

(5) Correct to eighth order in (J_1/kT) we find that $\chi_1(q)=\chi_{1,av}-(J_1/nkT)^8G(\mathbf{q})(n-1)/(n+2)^2$, where $\chi_{1,av}$ is independent of $\mathbf{q}$ [but does depend on (kT/J_1)] and $G(\mathbf{q})$ has a maximum at $\mathbf{q}=0$ and a minimum at the value of $\mathbf{q}$ corresponding to the $\sqrt{3}\times\sqrt{3}$ structure. The fact that $\mathbf{q}=0$ is favored for $n<1$ whereas the $\sqrt{3}\times\sqrt{3}$ state is favored for $n>1$, is quite plausible. $n=0$ corresponds to the self-avoiding-walk (SAW) problem, and we do not expect SAW's to exhibit the oscillatory behavior characteristic of sublattice formation. If the degeneracy is broken in favor of $\mathbf{q}=0$ for $n=0$ and is unbroken for $n=1$ at this order, it is plausible for it to be broken in favor of the $\sqrt{3}\times\sqrt{3}$ state for $n>1$. The fact that the $\sqrt{3}\times\sqrt{3}$ state has a finite entropy per site for $n>2$ would suggest that it is favored by finite temperature. However, a nonzero coupling between layers would be needed for true long-range order to actually occur.

(6) We give a useful and simple criterion which characterizes the removal of degeneracy. This criterion involves a sum with alternating sign of $\langle S(0)\cdot S(r)\rangle$ as $\mathbf{r}$ goes around a hexagon of sites. This sum is related to a local, soft-mode eigenvector which we found within spin-wave theory. This criterion can be used to extend the high-temperature analysis to include nonzero J_2 and J_3 and/or quantum corrections for finite S.

(7) The removal of degeneracy in $\chi_1(q)$ is nevertheless a small effect. Although we have demonstrated that, in principle, thermal fluctuations could conceivably lead to ground-state selection, in realistic situations, quantum interactions, further neighbor interactions, and other perturbations, such as dipole-dipole interactions, are likely to determine the structure. Thus the observed state may depend on the competition among small effects, as is the case in the copper oxide materials.[37]

(8) The fact that classically the $\sqrt{3}\times\sqrt{3}$ structure has a finite entropy per site suggests that quantum interactions give rise to an effective Hamiltonian within this degenerate manifold which describes a removal of degeneracy and thereby a nontrivial thermodynamics on a very small temperature scale. Preliminary results show that this effective interaction mimics an Ising model on a triangular lattice.

(9) Experimental measurements of the uniform static susceptibility are well modeled by our high-temperature expansion results. However, the fact that the data appear to follow a Curie-Weiss law is a bit misleading since the actual slope and intercept observed in Refs. 27 and 28 correspond to an intermediate-temperature regime and are not the values which would be expected if the true high-temperature regime were experimentally accessible.

(10) The peak in the elastic powder-neutron-diffraction data[28] says essentially nothing about whether $q=0$ or $\sqrt{3}\times\sqrt{3}$ order is preferred. This peak simply results from the fact that there are short-range antiferromagnetic correlations between spins on a kagomé lattice.

(11) Because of the very large degeneracy of the ground state of the pure kagomé system, it seems likely that even a small amount of dilution will stabilize a spin-glass-like state at low temperatures as is observed experimentally.[28]

Still open is the question of what happens in the quantum case, particularly for $S=\frac{1}{2}$ with nearest-neighbor interactions only. It is possible that the ground state is not of the Néel type for this case. A plausible alternative is some kind of dimer (spin Peierls) state, such as those discussed by Elser[26] and by Marston and Zeng.[38] It is possible to pair all of the spins in the kagomé lattice into valence bond (singlet) states. However, there are an infinite number of ways to do this, and it is not clear whether the system will freeze into a single structure, breaking translational symmetry, or whether it will resonate among different equivalent structures, remaining a spin liquid. High-temperature expansions, analogous to the one presented here, for the bond-bond susceptibility could shed some light on this problem.

ACKNOWLEDGMENTS

APPENDIX A

In this appendix we list the coupling constant matrices for the $\sqrt{3}\times\sqrt{3}$ structure, $\gamma_{\alpha,\beta}^{(n)}(\mathbf{k})$, $n=1,2$; $\alpha,\beta=1,\ldots,9$, which enter into Eqs. (2.8) and (2.27) and which are used to calculate the linear-spin-wave spectra:

$$\gamma_{\alpha,\alpha}^{(1)}(\mathbf{k})=8J_1-16J_2+8J_3 , \tag{A1}$$

$$\gamma_{1,2}^{(1)}(\mathbf{k})=J_1 e^{ik_x} , \tag{A2}$$

$$\gamma_{1,3}^{(1)}(\mathbf{k})=J_1 e^{i(k_x+\sqrt{3}k_y)/2} , \tag{A3}$$

$$\gamma_{1,4}^{(1)}(\mathbf{k})=J_3(e^{2ik_x}+e^{-i(k_x-\sqrt{3}k_y)}) , \tag{A4}$$

$$\gamma_{1,5}^{(1)}(\mathbf{k})=8J_2\cos\sqrt{3}k_y , \tag{A5}$$

$$\gamma_{1,6}^{(1)}(\mathbf{k})=J_1 e^{-i(k_x-\sqrt{3}k_y)/2} , \tag{A6}$$

$$\gamma_{1,7}^{(1)}(\mathbf{k})=J_3(e^{-2ik_x}+e^{i(k_x-\sqrt{3}k_y)}) , \tag{A7}$$

$$\gamma_{1,8}^{(1)}(\mathbf{k})=J_1 e^{-ik_x} , \tag{A8}$$

$$\gamma_{1,9}^{(1)}(\mathbf{k})=8J_2\cos[(3k_x+\sqrt{3}k_y)/2] , \tag{A9}$$

$$\gamma_{2,3}^{(1)}(\mathbf{k})=J_1 e^{-i(k_x-\sqrt{3}k_y)/2} , \tag{A10}$$

$$\gamma_{2,4}^{(1)}(\mathbf{k})=\gamma_{1,2}^{(1)}(\mathbf{k}) , \tag{A11}$$

$$\gamma_{2,5}^{(1)}(\mathbf{k})=J_3(e^{2ik_x}+e^{-i(k_x+\sqrt{3}k_y)}) , \tag{A12}$$

$$\gamma_{2,6}^{(1)}(\mathbf{k})=8J_2\cos[(3k_x-\sqrt{3}k_y)/2] , \tag{A13}$$

$$\gamma_{2,7}^{(1)}(\mathbf{k})=\gamma_{1,5}^{(1)}(\mathbf{k}) , \tag{A14}$$

$$\gamma_{2,8}^{(1)}(\mathbf{k})=J_3(e^{i(k_x+\sqrt{3}k_y)}+e^{-2ik_x}) , \tag{A15}$$

$$\gamma_{2,9}^{(1)}(\mathbf{k})=J_1 e^{i(k_x+\sqrt{3}k_y)/2} , \tag{A16}$$

$$\gamma_{3,4}^{(1)}(\mathbf{k})=\gamma_{1,9}^{(1)}(\mathbf{k}) , \tag{A17}$$

$$\gamma_{3,5}^{(1)}(\mathbf{k})=\gamma_{2,3}^{(1)}(\mathbf{k}) , \tag{A18}$$

$$\gamma_{3,6}^{(1)}(\mathbf{k})=J_3(e^{-i(k_x+\sqrt{3}k_y)}+e^{-i(k_x-\sqrt{3}k_y)}) , \tag{A19}$$

$$\gamma_{3,7}^{(1)}(\mathbf{k})=\gamma_{1,3}^{(1)}(\mathbf{k}) , \tag{A20}$$

$$\gamma_{3,8}^{(1)}(\mathbf{k})=\gamma_{2,6}^{(1)}(\mathbf{k}) , \tag{A21}$$

$$\gamma_{3,9}^{(1)}(\mathbf{k})=J_3(e^{i(k_x+\sqrt{3}k_y)}+e^{i(k_x-\sqrt{3}k_y)}) , \tag{A22}$$

$$\gamma_{\alpha,\beta}^{(1)}(\mathbf{k})=\gamma_{\alpha+3,\beta+3}^{(1)}(\mathbf{k})=\gamma_{\alpha+6,\beta+6}^{(1)}(\mathbf{k}), \quad \alpha,\beta=1,2,3 \tag{A23}$$

$$\gamma_{\beta,\alpha}^{(1)}(\mathbf{k})=\gamma_{\alpha,\beta}^{(1)}(\mathbf{k})^* , \tag{A24}$$

$$\gamma_{\alpha,\alpha}^{(2)}(\mathbf{k})=0 , \tag{A25}$$

$$\gamma_{\alpha,\beta}^{(2)}(\mathbf{k})=-(3/2)\gamma_{\alpha,\beta}^{(1)}(\mathbf{k}), \quad \alpha\neq\beta . \tag{A26}$$

For the case of nearest-neighbor interactions only, it is straightforward to show that the linear-spin-wave spectrum for the $\sqrt{3}\times\sqrt{3}$ structure is identical to that of the $q=0$ structure. Starting from Eq. (2.27) we first note that, for $J_2=J_3=0$, $[\gamma^{(1)},\gamma^{(2)}]=0$, and hence the dynamical matrix is simply

$$\Gamma_{\alpha,\beta}=\tfrac{1}{16}S^2[(\gamma^{(1)})^2-4(\gamma^{(2)})^2]_{\alpha,\beta} . \tag{A27}$$

For both structures,

$$\gamma_{\alpha,\beta}^{(1)}(\mathbf{k})=8J_1\delta_{\alpha,\beta}+J_1\tilde{\gamma}_{\alpha,\beta}^{(1)} , \tag{A28a}$$

$$\gamma_{\alpha,\beta}^{(2)}(\mathbf{k})=-\tfrac{3}{2}J_1\tilde{\gamma}_{\alpha,\beta}^{(1)} , \tag{A28b}$$

where, for the $q=0$ structure,

$$\tilde{\gamma}_{q=0}^{(1)}=2\Lambda , \tag{A29}$$

where Λ is defined in Eq. (2.12). For the $\sqrt{3}\times\sqrt{3}$ structure,

$$\tilde{\gamma}_{\sqrt{3}}^{(1)}=\begin{bmatrix} A & B & B^\dagger \\ B^\dagger & A & B \\ B & B^\dagger & A \end{bmatrix} , \tag{A30}$$

where

$$A = \begin{bmatrix} 0 & e^{iq_1} & e^{iq_2} \\ e^{-iq_1} & 0 & e^{-i(q_1-q_2)} \\ e^{-iq_2} & e^{i(q_1-q_2)} & 0 \end{bmatrix} , \qquad \text{(A31a)}$$

$$B = \begin{bmatrix} 0 & 0 & e^{-iq_2} \\ e^{iq_1} & 0 & 0 \\ 0 & e^{-i(q_1-q_2)} & 0 \end{bmatrix} , \qquad \text{(A31b)}$$

and $q_1 = k_x$, $q_2 = (k_x - \sqrt{3}k_y)/2$ as in Eq. (2.12). $\tilde{\gamma}^{(1)}_{\sqrt{3}}$ is reduced to block diagonal form by the unitary transformation

$$U = \frac{1}{\sqrt{3}} \begin{bmatrix} I & I & I \\ I & \omega I & \omega^2 I \\ I & \omega^2 I & \omega I \end{bmatrix} , \qquad \text{(A32)}$$

where I is a 3×3 unit matrix and $\omega = e^{2\pi i/3}$. The diagonal blocks of the transformed matrix are the 3×3 matrices $A + B + B^+$, $A + \omega B + \omega^2 B^+$, and $A + \omega^2 B + \omega B^+$. The first of these, $A + B + B^+$, is equal to $\tilde{\gamma}^{(1)}_{q=0}$ with q_1, q_2, and $q_1 - q_2$ cyclically permuted. The second two blocks are unitarily equivalent to $\Gamma(k \pm (2\pi/3)\hat{x})$. Thus the eigenvalues of $\tilde{\gamma}^{(1)}_{\sqrt{3}}$ are equal to those of $\tilde{\gamma}^{(1)}_{q=0}$ when the Brillouin zone of the $q=0$ structure is folded back into the $\sqrt{3} \times \sqrt{3}$ Brillouin zone.

APPENDIX B

In this appendix we give the calculations of the contributions C_d from diagram d labeled as in Fig. 11 where

$$C_d = \sum_{l=1}^{8} C_d^l y^l \qquad \text{(B1)}$$

and $y = \beta J/n$. We remind the reader that the dashed lines connecting vertices i and j indicate the presence of a factor $\mathbf{S}_i \cdot \mathbf{S}_j$. We start with diagram 1a, the one-step walk:

$$C_{1a} = \frac{\text{Tr}_{1,2}\mathbf{S}_1 \cdot \mathbf{S}_2 \exp(-ny\mathbf{S}_1 \cdot \mathbf{S}_2)}{\text{Tr}_{1,2}\exp(-ny\mathbf{S}_1 \cdot \mathbf{S}_2)} . \qquad \text{(B2)}$$

We introduce a convenient shorthand in which the trace operation on an operator A actually denotes a normalized trace: $\text{Tr} A/\text{Tr} 1$. With this convention we usually do not have to indicate which spins are being traced over. To evaluate C_{1a} we use

$$\text{Tr}(\mathbf{S}_i \cdot \mathbf{S}_j)^2 = 1/n , \qquad \text{(B2a)}$$

$$\text{Tr}(\mathbf{S}_i \cdot \mathbf{S}_j)^4 = 3/[n(n+2)] , \qquad \text{(B2b)}$$

$$\text{Tr}(\mathbf{S}_i \cdot \mathbf{S}_j)^6 = 15/[n(n+2)(n+4)] , \qquad \text{(B2c)}$$

$$\text{Tr}(\mathbf{S}_i \cdot \mathbf{S}_j)^8 = 105/[n(n+2)(n+4)(n+6)] . \qquad \text{(B2d)}$$

Thus, correct to order y,[7]

$$C_{1a} = \frac{-y - n^2y^3/2(n+2) - n^4y^5/8(n+2)(n+4) - n^6y^7/48(n+2)(n+4)(n+6)}{1 + ny^2/2 + n^3y^4/8(n+2) + n^5y^6/48(n+2)(n+4)} \qquad \text{(B3a)}$$

$$= -y + \frac{ny^3}{(n+2)} - \frac{2n^2y^5}{(n+2)(n+4)} + \frac{n^3(5n+12)y^7}{(n+2)^2(n+4)(n+6)} . \qquad \text{(B3b)}$$

Longer chain diagrams are easy to calculate. By relating the coordinate system for $\mathbf{S}_1$ to the direction of $\mathbf{S}_2$, one sees that

$$\text{Tr} \exp(-ny\mathbf{S}_1 \cdot \mathbf{S}_2)F(\mathbf{S}_2, \mathbf{S}_3, \ldots, \mathbf{S}_k)$$
$$= \text{Tr} \exp(-ny\mathbf{S}_1 \cdot \mathbf{S}_2)\text{Tr} F(\mathbf{S}_2, \mathbf{S}_3, \ldots, \mathbf{S}_k) \qquad \text{(B4a)}$$

and

$$\text{Tr} S_{1,\alpha}\exp(-ny\mathbf{S}_1 \cdot \mathbf{S}_2)F(\mathbf{S}_2, \mathbf{S}_3, \ldots, \mathbf{S}_k)$$
$$= \text{Tr}\mathbf{S}_1 \cdot \mathbf{S}_2 \exp(-ny\mathbf{S}_1 \cdot \mathbf{S}_2)\text{Tr} S_{2,\alpha}F(\mathbf{S}_2, \mathbf{S}_3, \ldots, \mathbf{S}_k) . \qquad \text{(B4b)}$$

Thus for a chain with k links (coming from diagram ka)

$$C_{ka} = (C_{1a})^k . \qquad \text{(B5)}$$

To evaluate the contributions from more complicated diagrams, we will invoke various relations. One is

$$\text{Tr} S^a S^b S^c S^d = \frac{1}{n(n+2)}(\delta_{a,b}\delta_{c,d} + \delta_{a,c}\delta_{b,d} + \delta_{a,d}\delta_{b,c}) , \qquad \text{(B6)}$$

where a, b, c, and d label Cartesian components. Consider the following quantity:

$$X \equiv \text{Tr}(\mathbf{S}_1 \cdot \mathbf{S}_2)^2(\mathbf{S}_2 \cdot \mathbf{S}_3)^2(\mathbf{S}_1 \cdot \mathbf{S}_3)^2 . \qquad \text{(B7)}$$

By using Eq. (B6) to perform the trace over, say, $\mathbf{S}_1$ one reduces X to a simple quantity. The result is then

$$X = \frac{n+8}{n^2(n+2)^2} . \qquad \text{(B8)}$$

Also we will need various cumulant averages, defined in Eq. (3.3). For example,

$$\text{Tr}[(\mathbf{S}_1 \cdot \mathbf{S}_2)^3 \mathbf{S}_1 \cdot \mathbf{S}_3 \mathbf{S}_2 \cdot \mathbf{S}_3]_c \equiv n^{-1}\text{Tr}[(\mathbf{S}_1 \cdot \mathbf{S}_2)^4]_c$$
$$= n^{-1}\{ \text{Tr}(\mathbf{S}_1 \cdot \mathbf{S}_2)^4$$
$$- 3[\text{Tr}(\mathbf{S}_1 \cdot \mathbf{S}_2)^2]^2\}$$
$$= -\frac{6}{n^3(n+2)} . \qquad \text{(B9)}$$

Next we consider the triangles. We start with the triangle with no appendages. We take the external vertices to be numbers 1 and 2. Then

$$C_{3b}^4 = \frac{n^4}{2}\mathrm{Tr}[(\mathbf{S}_1\cdot\mathbf{S}_2)^3\mathbf{S}_1\cdot\mathbf{S}_3\mathbf{S}_2\cdot\mathbf{S}_3]_c \tag{B10a}$$

$$= \frac{n^3}{2}\mathrm{Tr}[(\mathbf{S}_i\cdot\mathbf{S}_j)^4]_c = -\frac{3n}{(n+2)}. \tag{B10b}$$

Also

$$C_{3b}^5 = -\frac{n^5}{4}\mathrm{Tr}[(\mathbf{S}_1\cdot\mathbf{S}_2)^2(\mathbf{S}_1\cdot\mathbf{S}_3)^2(\mathbf{S}_2\cdot\mathbf{S}_3)^2]_c. \tag{B11}$$

Using the short-hand notation $T_{ij}\equiv\mathbf{S}_i\cdot\mathbf{S}_j$ we write Eq. (B11) as

$$\mathrm{Tr}[T_{12}^2T_{23}^2T_{13}^2]_c = \mathrm{Tr}T_{12}^2T_{23}^2T_{13}^2 - 3\,\mathrm{Tr}T^2\mathrm{Tr}T_{12}^2T_{23}^2$$

$$-4(\mathrm{Tr}T_{12}T_{23}T_{13})^2 + 2!(\mathrm{Tr}T^2)^3 \tag{B12}$$

$$= \mathrm{Tr}T_{13}^2\frac{1}{n(n+2)}(1+2T_{13}^2)$$

$$-\frac{3}{n^3}-\frac{4}{n^4}+\frac{2}{n^3}, \tag{B13}$$

where we used Eq. (B6) to obtain the first term in Eq. (B13). Also when subscripts are omitted on T it is because they do not matter. Thus

$$C_{3b}^5 = \frac{n(5n+4)}{(n+2)^2}. \tag{B14}$$

Next

$$C_{3b}^6 = \frac{n^6}{4!}\mathrm{Tr}(T_{12}^5T_{13}T_{23})_c + 2\frac{n^6}{3!2!}\mathrm{Tr}(T_{12}^3T_{13}^3T_{23})_c \tag{B15a}$$

$$= 5C_1^1C_1^5 + 6(C_1^3)^2 = \frac{10n^2}{(n+2)(n+4)}+\frac{6n^2}{(n+2)^2}. \tag{B15b}$$

In writing Eq. (B15b) we recognized the cumulants as being the same ones that would have risen for the linear chain had we analyzed it using cumulants.

Next

$$C_{3b}^7 = -\frac{2n^7}{2!4!}\mathrm{Tr}(T_{12}^2T_{13}^4T_{23}^2)_c - \frac{n^7}{2!2!3!}\mathrm{Tr}(T_{12}^4T_{13}^2T_{23}^2)_c \tag{B16a}$$

$$= -\frac{n^7}{12}\mathrm{Tr}(T_{12}^4T_{13}^2T_{23}^2)_c. \tag{B16b}$$

We evaluate this term as follows:

$$\mathrm{Tr}(T_{12}^4T_{13}^2T_{23}^2)_c = \mathrm{Tr}T_{12}^4T_{13}^2T_{23}^2 - 2\,\mathrm{Tr}T^2\mathrm{Tr}T_{12}^4T_{13}^2 - 6\,\mathrm{Tr}T^2\,\mathrm{Tr}T_{12}^2T_{13}^2T_{23}^2$$

$$- \mathrm{Tr}T^4\mathrm{Tr}T_{13}^2T_{23}^2 - 6\,\mathrm{Tr}T_{12}^2T_{13}^2\,\mathrm{Tr}T_{12}^2T_{23}^2 - 16\,\mathrm{Tr}T_{12}T_{23}T_{13}\mathrm{Tr}T_{12}^3T_{13}T_{23}$$

$$+ 2!24\,\mathrm{Tr}T^2(\mathrm{Tr}T_{12}T_{13}T_{23})^2 + 2!\,\mathrm{Tr}T^4(\mathrm{Tr}T^2)^2 + 2!(12)(\mathrm{Tr}T^2)^2\mathrm{Tr}T_{12}^2T_{13}^2$$

$$+ 2!(3)(\mathrm{Tr}T^2)^2\mathrm{Tr}T_{13}^2T_{23}^2 - 3!(3)(\mathrm{Tr}T^2)^4 \tag{B17}$$

$$= \mathrm{Tr}T_{12}^4\frac{1}{n(n+2)}(1+2T_{12}^2) - \frac{6}{n^3(n+2)} - \frac{6(n+8)}{n^3(n+2)^2} - \frac{3}{n^3(n+2)}$$

$$- \frac{6}{n^4} - \frac{48}{n^4(n+2)} + \frac{48}{n^5} + \frac{6}{n^3(n+2)} + \frac{24}{n^4} + \frac{6}{n^4} - \frac{18}{n^4}. \tag{B18}$$

So

$$C_{3b}^7 = -\frac{8n^2(7n+8)}{(n+2)^2(n+4)}. \tag{B19}$$

Finally, the mother of all triangles:

$$C_{3b}^8 = \frac{n^8}{6!}\mathrm{Tr}(T_{12}^7T_{13}T_{23})_c + \frac{n^8}{4!3!}(2)\mathrm{Tr}(T_{12}^5T_{13}^3T_{23})_c + \frac{n^8}{5!2!}(2)\mathrm{Tr}(T_{12}^3T_{13}^5T_{23})_c + \frac{n^8}{2!3!3!}\mathrm{Tr}(T_{12}^3T_{13}^3T_{23}^3)_c \tag{B20a}$$

$$= 7C_1^1C_1^7 + 10C_1^5C_1^3 + 6C_1^5C_1^3 + \frac{n^8}{72}\mathrm{Tr}(T_{12}^3T_{13}^3T_{23}^3)_c. \tag{B20b}$$

Now we need

$$Y \equiv \mathrm{Tr}(T_{12}^3T_{13}^3T_{23}^3)_c = \mathrm{Tr}T_{12}^3T_{23}^3T_{13}^3 - 9\,\mathrm{Tr}T^2\mathrm{Tr}T_{12}T_{23}^3T_{13}^3 - 27\,\mathrm{Tr}T_{12}T_{23}T_{13}\mathrm{Tr}T_{12}^2T_{23}^2T_{13}^2 - 27\,\mathrm{Tr}T_{12}^2T_{23}^2\,\mathrm{Tr}T_{12}T_{23}T_{13}^3$$

$$+ 2!(27)(\mathrm{Tr}T^2)^2\mathrm{Tr}T_{12}T_{23}T_{13}^3 + 2!(81)\mathrm{Tr}T^2\mathrm{Tr}T_{12}T_{23}T_{13}\mathrm{Tr}T_{12}^2T_{23}^2 + 2!(36)(\mathrm{Tr}T_{12}T_{23}T_{13})^3$$

$$- 3!(27)(\mathrm{Tr}T^2)^3\mathrm{Tr}T_{12}T_{23}T_{13}. \tag{B21}$$

By an extension of Eq. (B6) to the product of six operators we obtain

$$\text{Tr}(\mathbf{S}_1\cdot\mathbf{S}_2)^3(\mathbf{S}_1\cdot\mathbf{S}_3)^3(\mathbf{S}_2\cdot\mathbf{S}_3)^3 \tag{B22a}$$

$$= \frac{1}{n(n+2)(n+4)}\text{Tr}(\mathbf{S}_1\cdot\mathbf{S}_2)^3[9(\mathbf{S}_1\cdot\mathbf{S}_2)+6(\mathbf{S}_1\cdot\mathbf{S}_2)^3] \tag{B22b}$$

$$= \frac{1}{n(n+2)(n+4)}\left[\frac{90}{n(n+2)(n+4)}+\frac{27}{n(n+2)}\right] \tag{B22c}$$

$$= \frac{9(3n+22)}{n^2(n+2)^2(n+4)^2} \; . \tag{B22d}$$

Thus

$$\text{Tr}(T_{12}^3 T_{13}^3 T_{23}^3)_c = \frac{9(3n+22)}{n^2(n+2)^2(n+4)^2} - \frac{81}{n^3(n+2)^2} - \frac{27(n+8)}{n^4(n+2)^2} - \frac{81}{n^4(n+2)} + \frac{162}{n^4(n+2)} + \frac{162}{n^5} + \frac{72}{n^6} - \frac{162}{n^5} \tag{B23a}$$

$$= \frac{576(5n^2+12n+8)}{n^6(n+2)^2(n+4)^2} \; . \tag{B23b}$$

So

$$C_{3b}^8 = 7C_1^1 C_1^7 + 16C_1^3 C_1^5 + \frac{8n^2(5n^2+12n+8)}{(n+2)^2(n+4)^2} \tag{B24a}$$

$$= -\frac{7n^3(5n+12)}{(n+2)^2(n+4)(n+6)} - \frac{32n^3}{(n+2)^2(n+4)} + \frac{8n^2(5n^2+12n+8)}{(n+2)^2(n+4)^2} \tag{B24b}$$

$$= \frac{n^2}{(n+2)^2(n+4)^2(n+6)}[-7n(5n+12)(n+4)-32n(n+4)(n+6)+8(5n^2+12n+8)(n+6)] \tag{B24c}$$

$$= \frac{n^2}{(n+2)^2(n+4)^2(n+6)}(-27n^3-208n^2-464n+384) \; . \tag{B24d}$$

Now to the decorated triangles, starting with diagram 4b of Fig. 10. The free end is vertex 4 and the external vertex on the triangle is vertex number 1. So

$$C_{4b}^5 = -\frac{n^5}{2!}\text{Tr}(T_{12}^2 T_{13} T_{23} T_{24} T_{14})_c \tag{B25a}$$

$$= -\frac{n^4}{2}\text{Tr}(T_{14} T_{12}^3 T_{24})_c = -3C_1^1 C_1^3 \; , \tag{B25b}$$

$$C_{4b}^6 = \frac{n^6}{4}\text{Tr}(T_{14} T_{12} T_{13}^2 T_{23}^2 T_{24})_c = \frac{n^5}{4}\text{Tr}(T_{12}^2 T_{13}^2 T_{23}^2)_c \tag{B26a}$$

$$= -C_{3b}^5 = -\frac{n(5n+4)}{(n+2)^2} \; , \tag{B26b}$$

$$C_{4b}^7 = -\frac{n^7}{4!}\text{Tr}(T_{14} T_{12}^4 T_{13} T_{23} T_{24})_c - \frac{n^7}{3!2!}(2)\text{Tr}(T_{14} T_{12}^2 T_{13}^3 T_{23} T_{24})_2 - \frac{n^7}{3!2!}\text{Tr}(T_{14} T_{12}^2 T_{13} T_{23} T_{24}^3)_c \tag{B27a}$$

$$= -\frac{n^6}{4!}\text{Tr}(T_{14} T_{12}^5 T_{24})_c - \frac{n^6}{4}\text{Tr}(T_{12}^3 T_{13}^3 T_{23})_c \tag{B27b}$$

$$= -5C_1^1 C_1^5 - 9(C_1^3)^2 \; . \tag{B27c}$$

Lastly, for this cluster:

$$C_{4b}^8 = \frac{n^8}{2!4!}(2)\text{Tr}(T_{12} T_{13}^4 T_{23}^2 T_{24} T_{14})_c + \frac{n^8}{3!2!2!}\text{Tr}(T_{12}^3 T_{13}^2 T_{23}^2 T_{24} T_{14})_c + \frac{n^8}{3!2!2!}\text{Tr}(T_{12} T_{13}^2 T_{23}^2 T_{24}^3 T_{14})_c \tag{B28a}$$

$$= \frac{n^7}{24}\text{Tr}(T_{12}^2 T_{13}^4 T_{23}^2)_c + \frac{n^7}{24}\text{Tr}(T_{12}^4 T_{13}^2 T_{23}^2)_c + \frac{n^8}{24}\text{Tr}(T_{12}^3 T_{13}^2 T_{23}^2 T_{24} T_{14})_c$$

$$= \frac{n^7}{12}\text{Tr}(T_{12}^2 T_{23}^4 T_{23}^2)_c + \frac{n^8}{24}\text{Tr}(T_{12} T_{13}^2 T_{23}^2 T_{24}^3 T_{14})_c \; . \tag{B28b}$$

We evaluate the last term as

$$Y \equiv \mathrm{Tr}(T_{12}T_{13}^2 T_{23}^2 T_{24}^3 T_{14})_c = \mathrm{Tr}T_{12}T_{13}^2 T_{23}^2 T_{24}^3 T_{14} - \mathrm{Tr}T^2 \mathrm{Tr}T_{12}T_{23}^2 T_{24}^3 T_{14}$$

$$- \mathrm{Tr}T^2 \mathrm{Tr}T_{12}T_{13}^2 T_{24}^3 T_{14} - 3\,\mathrm{Tr}T^2 \mathrm{Tr}T_{12}T_{13}^2 T_{23}^2 T_{24}T_{14}$$

$$- 3\,\mathrm{Tr}T_{12}T_{24}T_{14}\,\mathrm{Tr}T_{13}^2 T_{23}^2 T_{24}^2 - 4\,\mathrm{Tr}T_{12}T_{23}T_{13}\mathrm{Tr}T_{13}T_{23}T_{24}^3 T_{14}$$

$$- \mathrm{Tr}T_{13}^2 T_{23}^2 \mathrm{Tr}T_{12}T_{24}^3 T_{14} - 3\,\mathrm{Tr}T_{13}^2 T_{24}^2 \mathrm{Tr}T_{12}T_{23}^2 T_{24}T_{14}$$

$$- 3\,\mathrm{Tr}T_{23}^2 T_{24}^2 \mathrm{Tr}T_{12}T_{13}^2 T_{24}T_{14} - 12\,\mathrm{Tr}T_{13}T_{32}T_{24}T_{41}\mathrm{Tr}T_{13}T_{12}T_{32}T_{24}^2$$

$$+ 2!(12)\mathrm{Tr}T_{13}T_{32}T_{24}T_{41}\mathrm{Tr}T^2 \mathrm{Tr}T_{13}T_{12}T_{32} + 2!(\mathrm{Tr}T)^2 \mathrm{Tr}T_{12}T_{24}^3 T_{14}$$

$$+ 2!(3)(\mathrm{Tr}T^2)^2 \mathrm{Tr}T_{12}T_{23}^2 T_{24}T_{14} + 2!(3)(\mathrm{Tr}T^2)^2 \mathrm{Tr}T_{12}T_{13}^2 T_{24}T_{14}$$

$$+ 2!(3)\mathrm{Tr}T^2 \mathrm{Tr}T_{12}T_{24}T_{14}\mathrm{Tr}T_{23}^2 T_{24}^2 + 2!(3)\mathrm{Tr}T^2 \mathrm{Tr}T_{12}T_{24}T_{14}\mathrm{Tr}T_{13}^2 T_{24}^2$$

$$+ 2!(3)\mathrm{Tr}T^2 \mathrm{Tr}T_{12}T_{24}T_{14}\mathrm{Tr}T_{13}^2 T_{23}^2 - 3!(3)(\mathrm{Tr}T^2)^3 \mathrm{Tr}T_{12}T_{14}T_{24} \tag{B29a}$$

$$= \frac{3(n+8)}{n^3(n+2)^3} - \frac{3}{n^4(n+2)} - \frac{3}{n^4(n+2)} - \frac{3(n+8)}{n^4(n+2)^2} - \frac{3}{n^5} - \frac{12}{n^5(n+2)} - \frac{3}{n^4(n+2)}$$

$$- \frac{3}{n^5} - \frac{3}{n^5} - \frac{12}{n^6} + \frac{24}{n^6} + \frac{6}{n^4(n+2)} + \frac{6}{n^5} + \frac{6}{n^5} + \frac{6}{n^5} + \frac{6}{n^5} + \frac{6}{n^5} - \frac{18}{n^5}, \tag{B29b}$$

where we used Eq. (B6) repeatedly for the first trace and Eq. (B8) for the fourth trace. Thus

$$Y = \frac{24(5n+4)}{n^6(n+2)^3}. \tag{B29c}$$

For the first term in Eq. (B28b) we use the result of Eq. (B19), so that

$$C_{4b}^8 = \frac{n^2(61n^2+200n+144)}{(n+2)^3(n+4)}. \tag{B30}$$

Next

$$C_{6b}^7 = C_{6c}^7 = -\frac{n^7}{2!}\mathrm{Tr}(T_{16}T_{12}T_{23}T_{34}T_{24}^2 T_{45}T_{56})_c \tag{B31a}$$

$$= -\frac{n^3}{2}\mathrm{Tr}(T_{24}^4)_c = \frac{3n}{(n+2)} \tag{B31b}$$

and

$$C_{6b}^8 = C_{6c}^8 = \frac{n^8}{4}\mathrm{Tr}(T_{16}T_{12}T_{23}^2 T_{34}^2 T_{24}T_{45}T_{56})_c \tag{B32a}$$

$$= -C_{3b}^5 = \frac{n^5}{4}\mathrm{Tr}(T_{23}^2 T_{34}^2 T_{24}^2)_c \tag{B32b}$$

$$= -\frac{n(5n+4)}{(n+2)^2}, \tag{B32c}$$

$$C_{5b}^6 = C_{5c}^6 = \frac{n^6}{2!}\mathrm{Tr}(T_{12}T_{23}T_{34}T_{45}T_{15}T_{24}^2)_c \tag{B33a}$$

$$= \frac{n^3}{2}\mathrm{Tr}(T_{24}^4)_c = -\frac{3n}{(n+2)}, \tag{B33b}$$

$$C_{5b}^7 = C_{5c}^7 = -\frac{n^7}{4}\mathrm{Tr}(T_{12}T_{23}^2 T_{34}^2 T_{24}T_{45}T_{15})_c \tag{B34a}$$

$$= -\frac{n^5}{4}\mathrm{Tr}(T_{23}^2 T_{34}^2 T_{24}^2)_c = \frac{n(5n+4)}{(n+2)^2}, \tag{B34b}$$

$$C_{5b}^8 = C_{5c}^8 = \frac{n^8}{4!}\mathrm{Tr}(T_{12}T_{23}T_{34}T_{45}T_{51}T_{24}^4)_c + \frac{2n^8}{3!2!}\mathrm{Tr}(T_{12}^3 T_{23}T_{34}T_{45}T_{51}T_{24}^2)_c + \frac{2n^8}{3!2!}\mathrm{Tr}(T_{12}T_{23}^3 T_{34}T_{45}T_{51}T_{24}^2)_c \tag{B35a}$$

$$= \frac{n^5}{4!}\mathrm{Tr}(T_{24}^6)_c + \frac{n^6}{3}\mathrm{Tr}(T_{12}^3 T_{24}^3 T_{14})_c \tag{B35b}$$

$$= \frac{n^2}{4!}\left[\frac{240}{(n+2)(n+4)} + \frac{288}{(n+2)^2}\right]. \tag{B35c}$$

Next

$$C_{7b}^8 = C_{7c}^8 = C_{7d}^8 = \frac{n^8}{2!}\mathrm{Tr}(T_{17}T_{12}T_{23}T_{34}T_{24}^2 T_{45}T_{56}T_{67})_c \tag{B36a}$$

$$= \frac{n^3}{2}\mathrm{Tr}(T_{24}^4)_c = -\frac{3n}{(n+2)}, \tag{B36b}$$

$$C_{6e}^7 = -\frac{n^7}{2!}\mathrm{Tr}(T_{12}^3 T_{23}T_{34}T_{45}T_{56}T_{16})_c \tag{B37a}$$

$$= -\frac{n^3}{2}\mathrm{Tr}(T_{12}^4)_c = \frac{3n}{(n+2)}, \tag{B37b}$$

and

$$C_{6e}^8 = 0 . \tag{B38}$$

For the hexagon when the external vertices are two steps apart:

$$C_{6f}^8 = \frac{n^8}{2!2!}\mathrm{Tr}(T_{13}T_{12}^2T_{23}^2T_{34}T_{45}T_{56}T_{16})_c \tag{B39a}$$

$$= \frac{n^5}{4}\mathrm{Tr}(T_{13}^2T_{12}^2T_{23}^2)_c = -C_{3b}^5 \tag{B39b}$$

$$= -\frac{n(5n+4)}{(n+2)^2} . \tag{B39c}$$

For the heptagon:

$$C_{7f}^8 = \frac{n^8}{2!}\mathrm{Tr}(T_{12}^3T_{23}T_{34}T_{45}T_{56}T_{67}T_{17})_c \tag{B40a}$$

$$= \frac{n^3}{2}\mathrm{Tr}(T_{12}^4)_c = -\frac{3n}{(n+2)} . \tag{B40b}$$

For the hexagon with a dangling bond:

$$C_{7e}^8 = \frac{n^8}{2!}\mathrm{Tr}(T_{17}T_{67}T_{16}^2T_{12}T_{23}T_{34}T_{45}T_{56})_c \tag{B41a}$$

$$= \frac{n^4}{2}\mathrm{Tr}(T_{17}T_{67}T_{16}^3)_c \tag{B41b}$$

$$= 3C_1^1C_1^3 = -\frac{3n}{(n+2)} . \tag{B41c}$$

For the two triangles:

$$C_{6d}^8 = \frac{n^8}{2!2!}\mathrm{Tr}(T_{12}T_{13}^2T_{14}T_{43}T_{35}T_{25}T_{23}^2)_c \tag{B42a}$$

$$= \frac{n^6}{4}\mathrm{Tr}(T_{12}T_{13}^3T_{23}^3)_c = 9(C_1^3)^2 = \frac{9n^2}{(n+2)^2} . \tag{B42b}$$

Finally, for the hexagon with triangle:

$$C_{8b} = n^8\mathrm{Tr}(T_{12}T_{23}T_{13}^2T_{34}T_{45}T_{56}T_{67}T_{17})_c \tag{B43a}$$

$$= n^3\mathrm{Tr}(T_{13}^4)_c \tag{B43b}$$

$$= -\frac{6n}{(n+2)} . \tag{B43c}$$

*Permanent address: Institute for Materials Research and Department of Physics, McMaster University, 1280 Main Street West, Hamilton, Ontario, Canada L83 4M1.

[1] F. Keffer, in *Handbuch der Physik XVIII/2*, edited by S. Flugge and H. P. Wijn (Springer, Berlin, 1966), p. 1.

[2] S. Chakravarty, B. I. Halperin, and D. R. Nelson, Phys. Rev. Lett. **60**, 1057 (1988).

[3] See, for example, I. Affleck, in *Fields, Strings and Critical Phenomena*, edited by E. Brézin and J. Zinn-Justin (North-Holland, Amsterdam, 1989).

[4] F. D. M. Haldane, Phys. Lett. **93A**, 464 (1983); Phys. Rev. Lett. **50**, 1153 (1983); J. Appl. Phys. **57**, 3359 (1985).

[5] I. Affleck, Nucl. Phys. **B257**, 397 (1985); Phys. Rev. Lett. **54**, 966 (1985); *ibid*. **56**, 408 (1986).

[6] E. Rastelli, A. Tassi, and L. Reatto, Physica B **97**, 1 (1979).

[7] N. Read and S. Sachdev, Phys. Rev. Lett. **66**, 1773 (1991); M. P. Gelfand, R. R. P. Singh, and D. A. Huse, Phys. Rev. B **40**, 10 801 (1989); S. Sachdev and N. Read, Int. J. Mod. Phys. B **5**, 219 (1991) and references therein.

[8] P. W. Anderson, Mater. Res. Bull. **8**, 153 (1973); V. Kalmeyer and R. B. Laughlin, Phys. Rev. Lett. **59**, 2095 (1987); Phys. Rev. B **39**, 11879 (1989).

[9] P. Chandra, P. Coleman, and A. I. Larkin, J. Phys. C **2**, 7933 (1990).

[10] D. S. Rokhsar, Phys. Rev. B **42**, 2526 (1990).

[11] A. B. Harris, A. J. Berlinsky, and C. Bruder, J. Appl. Phys. **69**, 5200 (1991).

[12] P. Weigmann, Phys. Rev. Lett. **60**, 821 (1988); X. G. Wen, F. Wilczek, and A. Zee, Phys. Rev. B **39**, 11413 (1989).

[13] G. Baskaran, Phys. Rev. Lett. **63**, 2524 (1989).

[14] D. A. Huse and V. Elser, Phys. Rev. Lett. **60**, 2531 (1988).

[15] R. Liebmann, *Statistical Mechanics of Periodic Frustrated Ising Systems* (Springer, Berlin, 1986).

[16] S. Miyashita, J. Phys. Soc. Jpn. **53**, 44 (1984) and references cited.

[17] J. N. Reimers, A. J. Berlinsky, and A.-C. Shi, Phys. Rev. B **43**, 865 (1991).

[18] J. N. Reimers (unpublished).

[19] J. Villian, R. Bidaux, J. P. Carton, and R. Conte, J. Phys. (Paris) **41**, 1263 (1980).

[20] E. Shender, Zh. Eksp. Teor. Fiz. **83**, 326 (1982) [Sov. Phys. JETP **56**, 178 (1982)].

[21] E. Rastelli and A. Tassi, J. Phys. C **20**, L303 (1987).

[22] M. E. Fisher and W. Selke, Phys. Rev. Lett. **44**, 1502 (1980); C. L. Henley, J. Appl. Phys. **61**, 3962 (1982); A. B. Harris, O. G. Mouritsen, and A. J. Berlinsky, Can. J. Phys. **62**, 915 (1984); A. Pimpinelli, G. Uimin, and J. Villain, J. Condens. Matt. **1**, 4693 (1991).

[23] A. Moreo, E. Dagatto, T. Jolicoeur, and J. Riera, Phys. Rev. B **42**, 6283 (1990); A. Chubukov, *ibid*. **44**, 392 (1991).

[24] C. Zeng and V. Elser, Phys. Rev. B **42**, 8436 (1990).

[25] D. S. Greywall and P. A. Busch, Phys. Rev. Lett. **62**, 1868 (1989); *ibid*. **65**, 2788 (1990); D. S. Greywall, Phys. Rev. B **41**, 1842 (1990).

[26] V. Elser, Phys. Rev. Lett. **62**, 2405 (1989).

[27] X. Obradors, A. Labarta, A. Isalgué, J. Tejada, J. Rodriquez, and M. Pernet, Solid State Commun. **65**, 189 (1988).

[28] C. Broholm, G. Aeppli, G. P. Espinosa, and A. S. Cooper, J. Appl. Phys. **67**, 5799(A) (1990); C. Broholm, G. Aeppli, G. Espinosa, and A. S. Cooper, Phys. Rev. Lett. **65**, 3173 (1990); A. P. Ramirez, G. P. Espinosa, and A. S. Cooper, *ibid*. **64**, 2070 (1990).

[29] M. G. Townsend, G. Longworth, and E. Roudaut, Phys. Rev. B **33**, 4919 (1986).

[30] M. Alba, J. Hammann, C. Jacobini, and C. Pappa, Phys. Lett. **89A**, 423 (1982); L. Bevaart, P. M. H. L. Tegelaar, A. J. van Duyneveldt, and M. Steiner, Phys. Rev. B **26**, 6150 (1982); C. Palla, J. Hammann, and C. Jacobini, J. Magn. Magn. Mater. **31-34**, 1391 (1983); C. Jacobini, thesis, Université de Paris VI, 1965 (unpublished); W. Kurtz and S. Roth, Physica **86-88B**, 715 (1977); W. Kurtz, R. Geller, H. Dachs, and P. Convert, Solid State Commun. **18**, 1479 (1976).

[31] M. A. Subramanian, C. C. Torardi, D. C. Johnson, J. Pannetier, and A. W. Sleight, J. Solid State Chem. **72**, 24 (1988); J. N. Reimers, J. E. Greedan, R. K. Kremer, E. Gmelin, and M. A. Subramanian, Phys. Rev. B **43**, 3387 (1991); J. E. Greedan, M. Sato, X. Yan, and F. S. Razavi, Solid State Commun. **59**, 895 (1986); J. N. Reimers and J. E. Greedan, J.

Solid State Chem. **72**, 390 (1988); J. N. Reimers, J. E. Greedan, S. L. Penny, and C. V. Stager, J. Appl. Phys. **67**, 5967 (1990); J. E. Greedan, J. N. Reimers, C. V. Stager, and S. L. Penny, Phys. Rev. B **43**, 5682 (1991).

[32] P. G. de Gennes, Phys. Lett. **38A**, 339 (1972).

[33] T. C. Hsu (private communication).

[34] To check our numerical work and at the same time to verify the condition for dispersionless $\chi_1(\mathbf{q})$, namely, that $M(\mathbf{R})$ vanish for hexagons not intersecting the origin, we modified the eighth-order data so as to satisfy this condition. With this modified data, there indeed was no dispersion in $\chi_1(\mathbf{q})$.

[35] G. Aeppli, C. Broholm, A. Ramirez, G. P. Espinosa, and A. S. Cooper, J. Magn. Magn. Mater. **90&91**, 255 (1990).

[36] The Padé Approximant, in *Theoretical Physics,* edited by G. A. Baker, Jr. and J. L. Gammel (Academic, New York, 1970).

[37] S. Skanthakumar, H. Zhang, T. W. Clinton, W.-H. Li, J. W. Lynn, Z. Fisk, and S. W. Cheong, Physica C **160**, 124 (1989); Y. Endoh, M. Matsuda, K. Yamada, K. Kakurai, Y. Hidaka, G. Shirane, and R. J. Birgeneau, Phys. Rev. B **40**, 7032 (1989).

[38] J. B. Marston and C. Zeng, J. Appl. Phys. **69**, 5692(B) (1991).